

TOI-6884b: A low-mass brown dwarf transiting a slightly evolved star

Akanksha Khandelwal^{1,2*}, Shubhendra Nath Das^{2,3}, Rishikesh Sharma², Abhijit Chakraborty², Churchil Dwivedi², Sanjay Baliwal², Karen A. Collins⁴, David W. Latham⁴, Allyson Bieryla⁴, Cristilyn N. Watkins⁴, Felipe Murgas^{5,6}, Norio Narita^{5,7,8}, Enric Pallé^{5,6}, Steve B. Howell⁹, Mark E. Everett¹⁰, Catherine A. Clark¹¹, Polina A. Budnikova¹², David Ciardi¹¹, Nikitha Jithendran², Akihiko Fukui^{5,7}, Ashirbad Nayak², Bob Massey¹³, Boris Safonov¹², Florence Libotte^{5,17}, Francis P. Wilkin¹⁴, Gregor Srdoc¹⁵, Howard M. Relles⁴, Ivan Bonilla-Mariana^{5,6}, Izuru Fukuda¹⁹, Jason D. Eastman⁴, Jerome de Leon⁷, Jesus Higuera¹⁰, Kapil Bharadwaj², Keith Horne¹⁶, Kendra Nguyen¹⁸, Kevikumar Lad², Manuel Pichardo Marcano¹, Micaela Magno¹⁴, Neelam JSSV Prasad², Noriharu Watanabe¹⁹, Richard P. Schwarz⁴, Sam Quinn⁴, Santiago Páez¹, Toshi Suganuma¹⁹, Y. Gómez Maqueo Chew¹

¹ Universidad Nacional Autónoma de México. Instituto de Astronomía. A.P. 70-264, 04510. Ciudad de México, México.

² Astronomy & Astrophysics Division, Physical Research Laboratory, Ahmedabad 380009, India

³ Indian Institute of Technology, 382355 Gandhinagar, India

⁴ Center for Astrophysics | Harvard & Smithsonian, 60 Garden Street, Cambridge, MA 02138, USA

⁵ Instituto de Astrofísica de Canarias (IAC), 38205 La Laguna, Tenerife, Spain

⁶ Departamento de Astrofísica, Universidad de La Laguna (ULL), E-38206 La Laguna, Tenerife, Spain

⁷ Komaba Institute for Science, The University of Tokyo, 3-8-1 Komaba, Meguro, Tokyo 153-8902, Japan

⁸ Astrobiology Center, 2-21-1 Osawa, Mitaka, Tokyo 181-8588, Japan

⁹ NASA Ames Research Center, Moffett Field, CA 94035, USA

¹⁰ NSF National Optical-Infrared Astronomy Research Laboratory, 950 N. Cherry Ave., Tucson, AZ 85719, USA

¹¹ NASA Exoplanet Science Institute, Caltech/IPAC, Pasadena, CA 91125, USA

¹² Lomonosov Moscow State University, Sternberg Astronomical Institute, Moscow, Russia

¹³ Villa '39 Observatory, Landers, CA 92285, USA

¹⁴ Department of Physics and Astronomy, Union College, 807 Union St., Schenectady, NY 12308, USA

¹⁵ Kotizarovci Observatory, Sarsoni 90, 51216 Viskovo, Croatia

¹⁶ SUPA Physics and Astronomy, University of St. Andrews, Fife, KY16 9SS, Scotland, UK

¹⁷ Sabadell Astronomical Society, Sabadell, Spain

¹⁸ Department of Astronomy, Yale University, 219 Prospect Street, New Haven, CT 06511, USA

¹⁹ Department of Multi-Disciplinary Sciences, Graduate School of Arts and Sciences, The University of Tokyo, 3-8-1 Komaba, Meguro, Tokyo 153-8902, Japan

Accepted XXX. Received YYY; in original form ZZZ

ABSTRACT

We report the discovery of a low-mass transiting brown dwarf orbiting TOI-6884 (TIC 156514476, $T_{\text{mag}} = 11.4$) from NASA's *Transiting Exoplanet Survey Satellite* (TESS) mission. The TESS light curves initially suggested an orbital period of ~ 14.42 days; however, our high-precision ground-based radial velocity measurements and multi-epoch time-series photometry reveal this to be a harmonic alias. We determine the true orbital period to be $4.808264^{+0.000015}_{-0.000014}$ days and confirm the substellar nature of the companion. TOI-6884b has a mass of $26.32^{+0.98}_{-0.93} M_{\text{J}}$, a radius of $0.927^{+0.51}_{-0.52} R_{\text{J}}$, and resides on a nearly circular orbit ($e = 0.067^{+0.010}_{-0.012}$). Its host star is a late F-type slightly evolved star with $M_{\star} = 1.410^{+0.075}_{-0.069} M_{\odot}$, $R_{\star} = 1.840^{+0.072}_{-0.073} R_{\odot}$, $\log g = 4.057^{+0.045}_{-0.039}$, $[\text{Fe}/\text{H}] = 0.094^{+0.073}_{-0.068}$ dex, and $T_{\text{eff}} = 6330^{+180}_{-160}$ K. TOI-6884b is a key addition to the small population of well-characterized transiting brown dwarfs orbiting host stars that have left the main sequence. The detection of such systems will contribute to our understanding of dynamical histories and structural evolution of short-period substellar companions around evolved stars.

Key words: Brown dwarfs – techniques: photometric – techniques: radial velocities – stars: individual: TOI-6884

1 INTRODUCTION

Brown dwarfs (BDs) are substellar objects that bridge the gap between giant planets and the lowest-mass hydrogen-burning stars.

* E-mail: akanksha@astro.unam.mx

They are commonly defined as occupying a mass range between the deuterium-burning limit at approximately $11\text{--}16 M_J$ and the onset of sustained hydrogen fusion near $75\text{--}80 M_J$ (Spiegel et al. 2011; Baraffe et al. 2002; Chabrier et al. 2023). The spread in these estimates can be explained by variations in metallicity, chemical composition, and formation conditions, reflecting the complex physics that governs their interiors. For example, at high metallicity (+0.5 dex), the hydrogen-burning minimum mass (HBMM) decreases to $\sim 66 M_J$ for hybrid atmosphere models and $\sim 70 M_J$ for cloud-free atmospheres (Morley et al. 2024).

Despite significant observational and theoretical efforts, the formation theories of BDs remain uncertain. It is suggested that they may form like stars via gravitational fragmentation of molecular clouds (Padoan & Nordlund 2004; Hennebelle & Chabrier 2008; Kratter & Lodato 2016) or within protoplanetary discs via core accretion or gravitational instability, analogous to giant planets (Alibert et al. 2005; Mordasini et al. 2009). This raises the possibility that BDs do not form a homogeneous population but instead exhibit a diversity of origins. Observational demographics support this hypothesis and indicate that formation pathways can influence the orbital properties of BD companions. Ma & Ge (2014) proposed a bifurcation in the BD population near $\sim 42.5 M_J$ based on orbital eccentricity distributions. Companions below this mass tend to show orbital architectures similar to giant planets (Rodríguez et al. 2023), whereas more massive BDs resemble stellar binaries in both eccentricity and period distributions (Halbwachs et al. 2003; Kiefer et al. 2021) (although see Schlaufman 2018 for an alternative proposed boundary). Subsequent studies with larger samples have generally supported this trend (Grieves et al. 2017, 2021; Kiefer et al. 2021; Page et al. 2024). In particular, the eccentricity distribution of short-period systems, where tidal interactions can circularize orbits, preserves crucial clues to the formation and migration history of these objects (Hut 1981; Adams & Laughlin 2006; Jackson et al. 2009; Beatty et al. 2018).

Given this, well-characterized BD companions are therefore essential benchmarks for understanding substellar physics. Transiting BDs are especially valuable because they enable direct, model-independent measurements of both mass and radius, yielding stringent tests of substellar structure and evolution (Burrows et al. 2011; Baraffe et al. 2015; Chabrier et al. 2000; Morley et al. 2024; Mukherjee et al. 2025). Measurements of mass and radius probe the mass–radius ($M - R$) relation, which is sensitive to age, atmospheric composition, equation of state, and thermal evolution. Comparisons between empirical mass–radius measurements and theoretical predictions have revealed phenomena such as radius inflation, metallicity effects, and cooling inefficiencies in some systems (Phillips et al. 2020; Page et al. 2024). As BDs lack sustained nuclear fusion, they cool and contract over time, making their observed properties sensitive probes of substellar evolution. Each new system with precisely determined parameters contributes significantly to constraining substellar models and helps in disentangling the roles of formation environment and evolution.

An additional layer of complexity arises when the host star evolves off the main sequence ($\log g > 4.1$ for main-sequence stars; Stassun et al. 2018). The evolution of a BD companion in this regime becomes particularly intriguing, yet BDs orbiting evolved stars remain poorly characterized due to observational challenges introduced by the large radii and strong radial-velocity jitter of their hosts (Yu et al. 2018; Tayar et al. 2019). Moreover, companions of evolved stars are expected to follow different evolutionary pathways compared to those orbiting main-sequence hosts, owing to stronger dynamical interactions (Veras 2016). For example, as the host star becomes more luminous, close-in companions receive increased irradiation, pro-

viding opportunities to study processes such as planetary inflation and re-inflation (e.g., Grunblatt et al. 2016; Saunders et al. 2022). At the same time, increased tidal forces can also cause faster orbital decay or even engulfment of the companion (Hut 1981; Jackson et al. 2008) which may induce the different eccentricity distribution seen in surviving hot Jupiters (Villaver et al. 2014; Grunblatt et al. 2018). Compared to planetary companions, BDs around evolved stars remain especially unexplored because only a small number of systems (~ 11) are known. Consequently, it is unclear whether BDs undergo orbital or structural changes analogous to those inferred for planets, highlights the need to expand the sample of well-characterized transiting BDs around evolved hosts.

In this work, we present the discovery and characterization of TOI-6884b, a transiting BD with a mass of $26.32^{+0.98}_{-0.93} M_J$, a radius of $0.927^{+0.51}_{-0.52} R_J$, and an age of $2.61^{+0.78}_{-0.75} \text{ Gyr}$, orbiting an F-type slightly evolved star with $T_{\text{eff}} = 6330^{+180}_{-160} \text{ K}$. The paper is organized as follows. In Section 2, we describe the observations. Section 3 presents our analysis and derived system parameters. In Section 4, we place TOI-6884b in the context of the known transiting BD population, with emphasis on the mass–radius relation and orbital eccentricity. Finally, we summarize our findings in Section 5.

2 OBSERVATIONS

2.1 TESS photometry

TOI-6884 (TIC 156514476, $T_{\text{mag}} = 11.4$) was observed by NASA’s *Transiting Exoplanet Survey Satellite* (TESS) in Sector 49 (UT 2022 February 26–March 25) with a 10-minute cadence on Camera 1 CCD 1. The star was initially flagged as a Community TESS Object of Interest (CTOI; Guerrero et al. 2021) by Nguyen et al. (2022), based on transit signals identified in the light curves extracted from the TESS Full Frame Images (FFIs) of Sector 49 using the TESS Science Processing Operations Center (SPOC) pipeline (Jenkins et al. 2016), and was subsequently alerted as a TESS Object of Interest (TOI) on 2024 February 1. We used the Pre-search Data Conditioning Simple Aperture Photometry (PDCSAP; Smith et al. 2012; Stumpe et al. 2014) light curves produced by the SPOC pipeline, which are publicly available via the Mikulski Archive for Space Telescopes (MAST)¹. These light curves were normalized and detrended using a Python package `ci.tlalique` (Barragán et al. 2021), which applies Gaussian Process regression to mitigate systematic effects and stellar variability. The resulting post-processed light curves are shown in Fig. 1. The TESS pipeline initially reported an orbital period of ~ 14.42 days. Upon careful inspection, we found that the first transit was present but not identified by the pipeline, producing a harmonic alias. Consequently, the true orbital period is approximately one-third of the initially reported value, as evident in the data (Fig. 1). A total of three transits are detectable in the data, while two additional events were missed due to spacecraft reorientation during data download.

Given the relatively large TESS pixel scale of $21''$ per pixel, contamination from nearby stars is possible. To assess this, we used the `tpfplotter` package (Aller et al. 2020) and the TESS-cont² algorithm (Castro-González et al. 2024) to examine sources within the SPOC aperture. Nearby stars with magnitude contrasts up to 8 could, in principle, mimic the shallower transit of TOI-6884.02 (Lillo-Box et al. 2014). Fig. 2 shows the TESS target pixel file and

¹ <https://mast.stsci.edu/portal/Mashup/Clients/Mast/Portal.html>

² Available at <https://github.com/castro-gzljz/TESS-cont>.

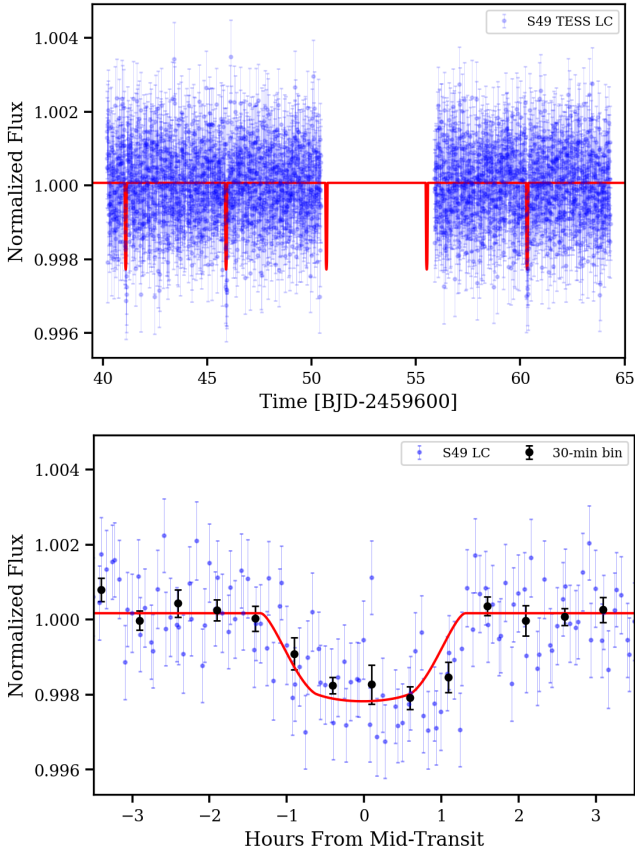


Figure 1. TESS light curve (LC) of TOI-6884 after detrending. The upper panel shows the full time-series LC, and the lower panel displays the phase-folded transit LC. Both panels include the best-fit transit model (red) and 30-minute binned data.

the SPOC pipeline aperture for Sector 49. Accounting for the relative positions of nearby sources and the TESS pixel response functions (PRFs), TESS-cont estimates that 99.98% of the flux in the aperture originates from TOI-6884. Therefore, the observed transit signal is intrinsic to the target star, and contamination from nearby sources can be confidently ruled out. Furthermore, the Gaia renormalized unit weight error (RUWE) for TOI-6884 is 1.22, consistent with a single-star astrometric solution (Gaia Collaboration et al. 2023).

To confirm the substellar nature of the companion and refine its orbital parameters, we conducted various ground-based follow-up observations, including high-precision radial velocity (RV) measurements and multi-epoch time-series photometry. The combination of TESS photometry and ground-based observations allowed us to determine the accurate orbital period, measure the companion’s mass and radius, and rule out potential false positive scenarios.

2.2 Ground-based Photometry

Ground-based time-series follow-up photometry of the field around TOI-6884 was obtained as part of the TESS Follow-up Observing Program (TFOP; Collins et al. 2017)³ to independently validate and refine the ephemerides of the 4.808-day orbital period. Transit observations were scheduled using the TESS Transit Finder, a

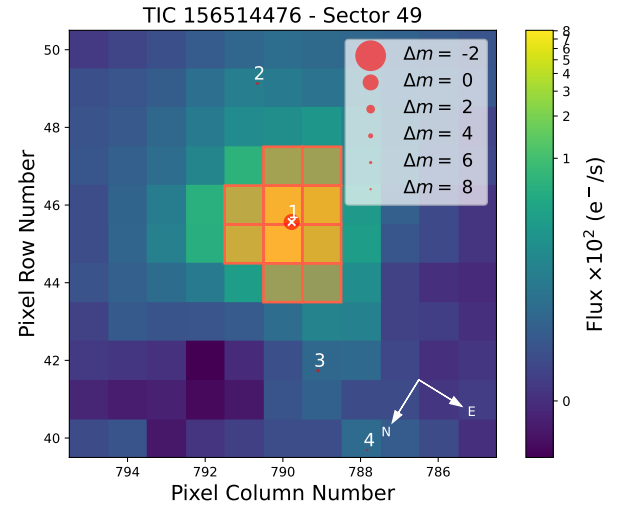


Figure 2. TESS target pixel file of TOI-6884 from Sector 49, generated with `tpfplotter` (Aller et al. 2020). The target star is marked with a white cross and labeled as 1. Nearby Gaia DR3 sources within a magnitude contrast of $\Delta m \leq 8$ are shown as red circles, with symbol sizes scaled by relative brightness. The SPOC photometric aperture is indicated by the shaded red pixels.

customized implementation of the `Tapir` software package (Jensen 2013). All light curve data are available on the EXOFOP-TESS website⁴ and are summarized in Table 1 and included in the global modelling described in section 3.5 and also see Fig. 3.

2.2.1 LCOGT

We observed one full and two partial transit windows of TOI-6884.01 on UT 2024 April 5, 2024 April 24, and 2024 April 29 in Sloan i' from the Las Cumbres Observatory Global Telescope (Brown et al. 2013, LCOGT) 1 m network node at McDonald Observatory near Fort Davis, Texas, United States (McD). The 1 m telescopes are equipped with a 4096×4096 SINISTRO camera having an image scale of $0''.389$ per pixel, resulting in a $26' \times 26'$ field of view. We observed another partial transit window on UT 2024 February 12 from the LCOGT 0.35 m network node at Teide Observatory on the island of Tenerife (TEID). The 0.35 m Planewave Delta Rho 350 telescope is equipped with a 9576×6388 QHY600 CMOS camera having an image scale of $0''.73$ per pixel, resulting in a $114' \times 72'$ field of view. However, the image data were collected using the $30' \times 30'$ central field of view sub-frame mode. Finally, we observed a full transit with limited pre-ingress baseline coverage on UT 2024 December 25 from the LCOGT 2 m Faulkes Telescope North at Haleakala Observatory on Maui, Hawai'i. The 2 m LCOGT telescope is equipped with the MuSCAT3 multi-band imager (Narita et al. 2020). All images were calibrated by the standard LCOGT BANZAI pipeline (McCully et al. 2018), and differential photometric data were extracted using `AstroImageJ` (Collins et al. 2017). We used circular photometric apertures with radii $4''.3$ to $7''.3$ that excluded all of the flux from the nearest known neighbor in the Gaia DR3 catalog (Gaia DR3 3961540708410542592) that is $71''.1$ southeast of TOI-6884.

³ <https://tess.mit.edu/followup>

⁴ <https://exofop.ipac.caltech.edu/tess/target.php?id=156514476>

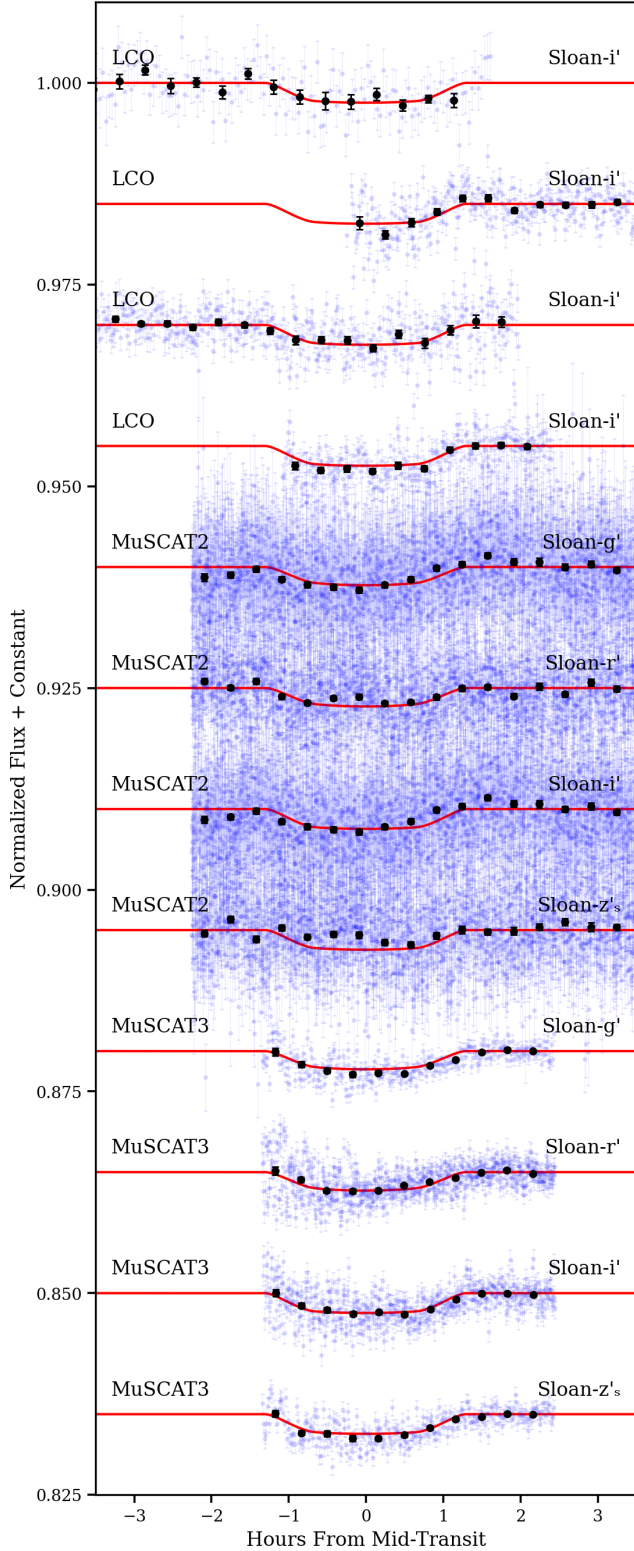


Figure 3. Transit light curves of TOI-6884 from our follow-up observations with MuSCAT-2 and LCOGT 1 m, 0.35 m, and 2 m MuSCAT-3. All the dataset are 20-minutes binned. The solid red line represents the best-fit transit model generated with the *batman* package (Kreidberg 2015), using the parameters from the most probable EXOFASTv2 solution (the high-mass fit, $\text{Pr} \sim 77\%$). Details of the observational parameters are listed in Table 1.

2.2.2 MuSCAT2

A full transit of TOI-6884.01 was observed on UT 2024 May 3 with MuSCAT2 (Narita et al. 2019), a four-channel imager mounted on the 1.5 m Telescopio Carlos Sánchez (TCS) at the Teide Observatory, Spain. MuSCAT2 enables simultaneous imaging in the g' , r' , i' , and z_s bands using four 1024×1024 CCDs, each covering a field of view of $7.4' \times 7.4'$.

The observations were carried out with the telescope in nominal focus. Exposure times of 8 s in g' and 10 s in r' , i' , and z_s were adopted. The data were reduced using the MuSCAT2 pipeline (Parviainen et al. 2019), which performs dark subtraction, flat-field correction, aperture photometry, and a simultaneous fit of the transit model and instrumental systematics, while selecting the best aperture for the time series. The transit signal was clearly detected in the photometry of the target star.

2.3 PARAS-2 radial velocities

The RV observations were taken using the PARAS-2 (Chakraborty et al. 2018; Chakraborty et al. 2024) high-resolution spectrograph attached to PRL 2.5 m telescope situated at the Mount Abu Observatory, Rajasthan, India. PARAS-2 is a high-resolution ($R \approx 110,000$) echelle-based spectrograph maintained in a highly temperature- and pressure-stable environment and works in the wavelength range of 380–690 nm. This spectrograph uses simultaneous observations from Uranium-Argon hollow cathode lamps for precise measurements of instrumental drifts. This instrument has shown an on-sky stability of 2.65 m s^{-1} over more than a month on a RV standard star (Baliwal et al. 2024). We have computed the RV values by performing cross-correlation of the observed spectrum with a template spectrum Baranne et al. (1996). One can refer to Baliwal et al. (2024) for a detailed discussion of the data reduction and the analysis of the science observations taken with PARAS-2. We have taken a total of 20 spectroscopic observations with 3600 seconds of exposure time, spanning over 68 days from 2024 February 15 to 2024 April 22. In those 26 spectroscopic observations, we have obtained per pixel signal to noise ratios ranging from 9 to 30 at 550 nm with a median value of 14. The photon noises in the RVs range from 48.22 m s^{-1} to 167.58 m s^{-1} , with a median value of 83.15 m s^{-1} . The calculation of the photon noise is based on the methods mentioned in Chaturvedi et al. (2016). All the details of the RV observations for TOI-6884 are listed in Table 2.

2.4 TRES radial velocities

The RV observations were obtained between February and April 2024 using the Tillinghast Reflector Echelle Spectrograph (TRES; Fűrész 2008), mounted on the 1.5 m Tillinghast Reflector telescope at the Fred Lawrence Whipple Observatory (FLWO) atop Mount Hopkins, Arizona. TRES is an optical, fiber-fed echelle spectrograph with a wavelength coverage of 390–910 nm and a resolving power of $R \sim 44,000$. The spectra were obtained in sequences of three exposures bracketed by ThAr calibration spectra, and the median of each sequence was combined to remove cosmic rays. The average exposure time was ~ 1100 s, resulting in an average signal-to-noise ratio per resolution element of 36.1. The spectra were extracted following the procedure described in Buchhave et al. (2010). A multi-order analysis was then performed by cross-correlating each spectrum, order by order, against a co-added template spectrum to determine the RVs. The RVs derived from the TRES spectra, along with their associated uncertainties, are listed in Table 2.

Table 1. A summary of the ground-based transit follow-up observations

Target	Telescope	Date	Filter	Exposure Time (s)	Photometric Aperture (″)
TOI-6884.01	LCO/Teid	Feb 11 2024	Sloan- <i>i'</i>	155	8.1
TOI-6884.01	LCO/McD	Apr 5 2024	Sloan- <i>i'</i>	52	5.8
TOI-6884.01	LCO/McD	Apr 24 2024	Sloan- <i>i'</i>	54	4.3
TOI-6884.01	LCO/McD	Apr 29 2024	Sloan- <i>i'</i>	52	3.9
TOI-6884.01	TCS/MuSCAT-2	May 3 2024	Sloan- <i>g'r'u'z'_s</i>	11	10.9
TOI-6884.01	LCO-HAL/MuSCAT-3	Dec 25 2024	Sloan- <i>g'r'u'z'_s</i>	53	7.2

Table 2. Radial velocity measurements of TOI-6884 from PARAS-2 and TRES. Column 1 lists the barycentric Julian dates (BJD_{TDB}) of the observations, followed by the relative RVs and their associated uncertainties (Columns 2 and 3). Columns 4 and 5 give the bisector velocity spans and their corresponding uncertainties. The exposure times are provided in Column 6, and the final column identifies the instrument used for each observation.

BJD_{TDB} (days)	RV (m s^{-1})	σ_{RV} (m s^{-1})	BIS (m s^{-1})	σ_{BIS} (m s^{-1})	Exp. time (s)	Instrument
2460356.475724	472.99	42.75	-938.47	109.53	3600	PARAS-2
2460368.474969	-4475.52	68.77	-24.67	143.20	3600	PARAS-2
2460376.479988	-1240.04	103.68	-1218.89	422.15	3600	PARAS-2
2460383.418293	-3739.71	77.87	-304.96	278.01	3600	PARAS-2
2460384.413929	-1215.37	81.47	756.28	243.66	3600	PARAS-2
2460386.405985	-2548.83	149.11	-442.40	288.97	3600	PARAS-2
2460387.426305	-4238.95	77.03	-577.17	415.28	3600	PARAS-2
2460388.305673	-3871.34	110.86	-112.64	244.50	3600	PARAS-2
2460392.369709	-4052.31	118.13	-1232.28	552.41	3600	PARAS-2
2460398.354432	-2420.79	167.58	-2000.00	519.55	3600	PARAS-2
2460401.213912	-3730.36	90.40	-1495.61	534.65	3600	PARAS-2
2460407.305667	-4523.26	99.05	311.32	842.42	3600	PARAS-2
2460408.247688	-1933.01	94.35	-2781.35	577.45	3600	PARAS-2
2460408.320533	-2545.80	61.43	-1842.09	178.89	3600	PARAS-2
2460409.343806	591.15	65.18	-1783.32	217.96	3600	PARAS-2
2460419.260935	-1179.37	48.22	-414.71	254.16	3600	PARAS-2
2460419.311072	-572.84	63.52	817.49	195.06	3600	PARAS-2
2460420.202738	-2381.70	102.58	-205.40	1431.03	3600	PARAS-2
2460420.293521	-2740.45	66.52	136.94	187.33	3600	PARAS-2
2460423.319249	-493.88	84.82	1398.94	530.77	3600	PARAS-2
2460355.881282	1784.20	47.80	720	TRES
2460356.934107	1818.80	36.80	960	TRES
2460362.822458	-1659.80	41.60	1200	TRES
2460374.862271	1200.40	24.60	1050	TRES
2460386.849183	-1713.50	40.10	1400	TRES
2460387.878980	-2319.90	32.30	800	TRES
2460388.817584	-41.30	33.50	900	TRES
2460390.865991	1149.50	34.80	900	TRES
2460399.774034	2327.40	33.60	1700	TRES
2460403.824561	1476.80	52.00	900	TRES
2460405.916145	-1237.90	40.80	1250	TRES
2460408.813021	1867.70	42.40	1500	TRES

2.5 High-angular-resolution imaging

If a host star has a spatially close companion, that companion (bound or line of sight, e.g., an EB) can create a false-positive transit signal. “Third-light” flux from the close companion star can lead to an underestimated planetary radius if not accounted for in the transit model (Ciardi et al. 2015), cause non-detections of small planets residing with the same exoplanetary system (Lester et al. 2021), and cause the derivation of incorrect exoplanet and star properties (Furlan & Howell 2017, 2020). Additionally, the discovery of close, bound companion stars, which exist in nearly one-half of FGK type stars (Matson et al. 2018), provides crucial information toward our

understanding of exoplanetary formation, dynamics and evolution (Howell et al. 2021). Thus, to search for close-in bound companions unresolved in TESS observations, we performed ground-based high-resolution follow-up observations of TOI-6884.

2.5.1 Gemini observations

TOI-6884 was observed on UT 2024 March 22 using the ‘Alopeke speckle instrument on the Gemini North 8 m telescope (Scott et al. 2021). ‘Alopeke provides simultaneous speckle imaging in two bands (562 nm and 832 nm) with output data products including a reconstructed image with robust contrast limits on companion detections.

[ht!]

Table 3. Astrometry, photometry, and kinematics properties of TOI-6884.

Parameter	Value	Ref.
Identifiers:		
TIC	156514476	(1)
2MASS	J12520212+2640262	(3)
GaiaDR3	3961540914568972928	(4)
Astrometry:		
α_{J2000}	12:52:02.11	(4)
δ_{J2000}	26:40:26.22	(4)
μ_α (mas yr ⁻¹)	10.544 ± 0.022	(4)
μ_δ (mas yr ⁻¹)	-21.279 ± 0.017	(4)
ϖ^* (mas)	4.727 ± 0.021	(4)
d (pc)	211.53 ^{+0.94} _{-0.93}	(4)
Photometry*:		
B_T	11.024 ± 0.046	(2)
V_T	10.315 ± 0.034	(2)
T	9.6089 ± 0.0062	(1)
G	10.045 ± 0.020	(4)
G_{BP}	10.370 ± 0.020	(4)
G_{RP}	9.558 ± 0.020	(4)
J	9.022 ± 0.029	(3)
H	8.736 ± 0.031	(3)
K_S	8.684 ± 0.020	(3)
$W1$	8.648 ± 0.030	(5)
$W2$	8.691 ± 0.030	(5)
$W3$	8.650 ± 0.030	(5)
$W4$	8.658 ± 0.288	(5)
Kinematics:		
U, V, W (km s ⁻¹)	-31.203, -4.316, -13.763	(6)
$U_{LSR}, V_{LSR}, W_{LSR}$ (km s ⁻¹)	-20.103, 7.924, -6.513	(6)

*A systematic error floor has been applied to the uncertainties.

References: (1) [Stassun et al. \(2018\)](#), (2) [Høg et al. \(2000\)](#),
(3) [Cutri et al. \(2003\)](#), (4) [Gaia Collaboration et al. \(2023\)](#),
(5) [Cutri et al. \(2021\)](#), (6) This work

Nine sets of 1000 X 0.06 seconds exposures were collected and subjected to Fourier analysis in our standard reduction pipeline (see [Howell et al. 2011](#)). Fig. 4 shows our final contrast curves and the 832 nm reconstructed speckle image. We find that TOI-6884 is a single star with no companion star brighter than the 4.5 to 6.5 5σ magnitude contrast below that of the target star from the diffraction limit (20 mas) out to 1.2". At the distance of TOI-6884 ($d=562$ pc) these angular limits correspond to spatial limits of 11 to 674 au.

2.5.2 Palomar observations

TOI-6884 was observed on 2024 February 15 using the Palomar High Angular Resolution Observer (PHARO) instrument ([Hayward et al. 2001](#)) mounted on the 5 m Hale Telescope at Palomar Observatory. Observations were carried out behind the natural guide star P3K AO system ([Dekany et al. 2013](#)) using the narrowband K_{cont} filter ($\lambda_0 = 2.26 \mu\text{m}$, $\Delta\lambda = 0.06 \mu\text{m}$). PHARO provides a pixel scale of 0.025" per pixel. The observations consisted of images obtained in sets of 15 following a standard five-point quincunx dither pattern with 5" offsets, repeated three times, with each repeat separated by 0.5". The reduced science frames were combined to produce a single mosaicked image with a final angular resolution of 0.10". The sensitivity of the final combined AO image was assessed by injecting simulated point sources azimuthally around the primary star

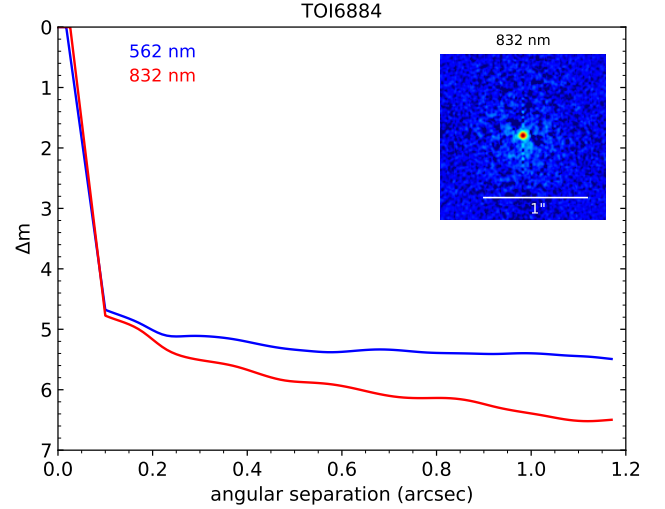


Figure 4. Speckle imaging observations of TOI-6884 obtained with ‘Alopec’ at the Gemini North telescope. The magnitude contrast curves represent fits to the 5σ detection limits from the diffraction limit out to the edge of the field of view. The inset panel shows the reconstructed image at 832 nm.

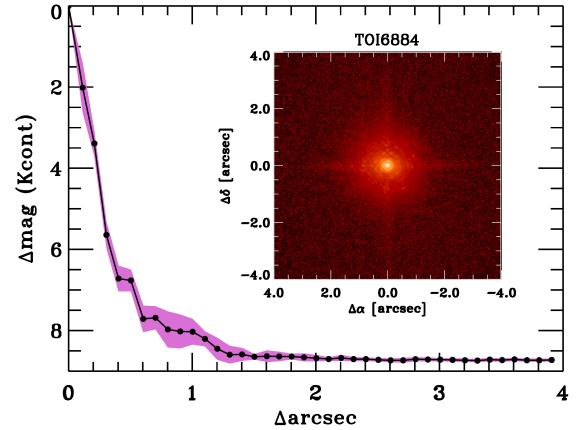


Figure 5. Palomar near-infrared AO imaging and sensitivity curves for TOI-6884 taken in the K_{cont} filter. Inset: Image of the central portion of the data, centered on the star.

at position angles spaced every 20°, and at separations corresponding to integer multiples of the FWHM of the central source, following the methodology of [Furlan et al. \(2017\)](#). The flux of each injected source was scaled until it was detected at a 5σ significance level using standard aperture photometry. At each separation, the final 5σ contrast limit was determined as the average of the recovered limits across all azimuthal angles, with uncertainties calculated from the rms dispersion of the azimuthal measurements. The resulting contrast curve is shown in Fig. 5. No companion was detected around TOI-6884 down to a contrast of $\Delta K = 8.0$ mag relative to the primary star at separations out to 1.0".

2.5.3 SAI observations

TOI-6884 was observed on UT 2024 February 27 with the speckle polarimeter on the 2.5 m telescope at the Caucasian Observatory of

Sternberg Astronomical Institute (SAI) of Lomonosov Moscow State University. A low-noise CMOS detector Hamamatsu ORCA-quest (Strakhov et al. 2023) was used as a detector. The atmospheric dispersion compensator was active, which allowed using the I_c band. The respective angular resolution is $0.083''$. A total of 6292 frames with 19 ms exposure have been accumulated. The long-exposure FWHM was $0.81''$. We did not detect any stellar companions, detection limits are $\Delta I_c = 3.8^m$ and 5.5^m at distances 0.25 and $1.0''$ from the star, respectively. Fig. A1a shows our final contrast curve.

2.5.4 WIYN observations

We observed TOI-6884 using speckle imaging on UT 2024 February 17 with the NN-EXPLORE Exoplanet Stellar Speckle Imager (NESSI; Scott et al. 2018) at the WIYN 3.5 m telescope on Kitt Peak. NESSI obtains simultaneous speckle imaging in two filters. In this case, the filters had central wavelengths $\lambda_c = 562$ and 832 nm. Our observation consisted of a set of 9 1000-frame 40 ms exposures. The field-of-view was limited by reading out a 256×256 pixel subsection of the CCDs, resulting in 4.6×4.6 arcsecond images. Our speckle measurements were further restricted to an outer radius of 1.2 arcseconds from the target star, an area inside of which the speckle patterns were correlated. A similar observation of a point source standard star was taken in conjunction with that of the TOI. The standard observation consisted of a single 1000-frame image set and was used to calibrate the intrinsic PSF. The speckle data were reduced using a pipeline process documented by Howell et al. (2011). Among the pipeline products are reconstructed images of the field around TOI-6884 in each filter. We used these to measure contrast curves, setting detection limits on any point sources close to the TOI (see Fig. A1b). No companion sources were detected near TOI-6884.

3 ANALYSIS AND RESULTS

3.1 Spectroscopic parameters from spectral synthesis

The TRES spectra were also used to derive spectroscopic parameters of TOI-6884 with the Stellar Parameter Classification tool (SPC; Buchhave et al. 2012). SPC cross-correlates each observed spectrum against a grid of synthetic spectra based on the Kurucz atmospheric models (Kurucz 1992). We used all 12 TRES spectra. The average stellar parameters derived with T_{eff} , $\log g$, $[\text{m}/\text{H}]$, and $\nu \sin i$ as free parameters are: $T_{\text{eff}} = 6201 \pm 53$ K, $\log g = 4.16 \pm 0.10$, $[\text{m}/\text{H}] = 0.05 \pm 0.08$, $\nu \sin i = 12.9 \pm 0.5$ km s $^{-1}$, with a typical signal-to-noise per resolution element (SNRe) of 36.1.

3.2 Stellar Rotation Period and Photometric Modulation

We searched for photometric modulation in the *TESS* SAP light curve using out-of-transit data, excluding data with non-zero quality flags as indicated by the SPOC pipeline. We computed a Generalized Lomb-Scargle (GLS; Zechmeister, M. & Kürster, M. 2009) periodogram, which reveals a periodic signal at 6.89 ± 0.05 days (see Fig. 6). However, this signal is not independently confirmed in data from the SuperWASP all-sky survey (SWASP; Butters et al. 2010).

TOI-6884 is a moderately rotating star, with a projected rotational velocity of $\nu \sin i = 12.9 \pm 0.5$ km s $^{-1}$ as derived from SPC. The stellar inclination can be estimated by combining the stellar radius, rotation period, and projected rotational velocity. Using the stellar radius ($R_* = 1.840^{+0.072}_{-0.073} R_\odot$) from our global modeling (Section 3.5), the photometric rotation period, and the spectroscopic $\nu \sin i$, and

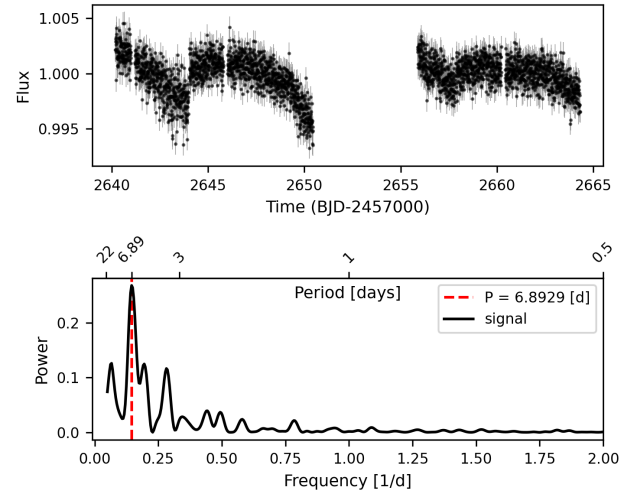


Figure 6. Top panel: *TESS* SAP light curve of TOI-6884, showing the out-of-transit photometric data used for rotation period measurement. Bottom panel: GLS periodogram of the light curve. The vertical dashed red line marks the detected periodic signal at $P = 6.89$ days. The upper axis shows the corresponding period scale.

neglecting differential rotation, we estimate a stellar inclination of $72.70 \pm 10.29^\circ$ following Masuda & Winn (2020). The orbital inclination derived from the global modeling is $i = 82.46^{+0.45}_{-0.42}^\circ$, suggesting that the system is likely consistent with alignment between the brown dwarf orbital axis and the stellar spin axis.

3.3 Galactic Kinematics

We estimated the Galactic space velocity components (U , V , W) in the barycentric reference frame using the `gal_uv`⁵ function. The resulting velocities, reported in Table 3, follow the convention that U is positive toward the Galactic center, V in the direction of Galactic rotation, and W toward the north Galactic pole. We also computed velocities relative to the local standard of rest (LSR) by adopting the solar motion values from Schönrich et al. (2010), which are also provided in Table 3. Based on our analysis, the kinematics of TOI-6884 are consistent with membership in the Galactic thin disk (Leggett 1992; Bensby et al. 2014). In addition, we used the BANYAN Σ tool, which evaluates membership probabilities based on sky position, proper motion, parallax, and radial velocity, and it classifies TOI-6884 as a field star with a probability greater than 99%, with no association to any known young stellar group (Gagné et al. 2018).

3.4 Periodogram analysis of RVs

We computed the GLS for the RVs, residual RVs, window function, FWHM, and bisector span (BIS), shown in panels 1 through 5 (top to bottom) of Fig. 7, respectively. The periodogram analysis was performed on RVs obtained from the PARAS-2 spectrograph, following the normalization and false alarm probability (FAP) calculation methods described in Zechmeister, M. & Kürster, M. (2009).

⁵ https://pyastronomy.readthedocs.io/en/latest/pyaslDoc/aslDoc/gal_uv.html

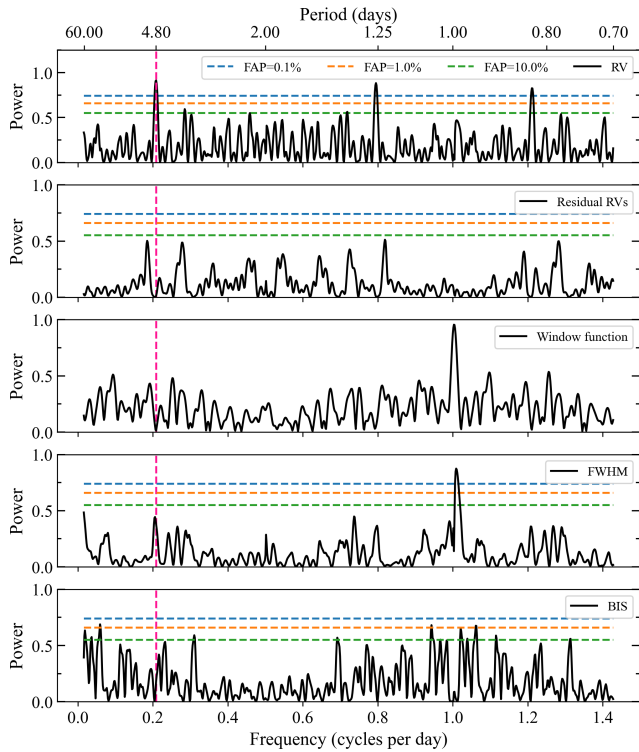


Figure 7. GLS periodograms of TOI-6884. From top to bottom: (1) Radial velocities, (2) Residual RVs after subtracting the dominant signal, (3) Window function, (4) FWHM, and (5) Bisector span. The primary peak at a period of ≈ 4.82 days (magenta dashed line) corresponds to the photometrically derived orbital period of the planetary candidate. False alarm probability levels of 0.1%, 1%, and 10% are indicated as horizontal dashed lines.

Adopting a significance threshold of 0.1% FAP, we identify a prominent peak at a period of $\approx 4.82 \pm 0.02$ days (indicated by the vertical dashed line in Fig. 7), consistent with the orbital period derived from both ground- and space-based transit observations of this planetary candidate.

In addition to the primary planetary signal, the RV periodogram exhibits three other significant peaks at periods of 1.26, 0.82, and 0.56 days. These signals disappear when the ≈ 4.82 -day periodic component is removed using a best-fit sinusoidal model, as evidenced by the clean residual periodogram in panel 2. We attribute these spurious signals to the aliases of the orbital frequency or the 4.82 days signal: the $1/0.82$ represents the 1-day alias of f_{orb} , whereas, the $1/1.26$ and $1/0.56$ signals correspond to the 1-day and 2-day aliases of $-f_{\text{orb}}$ respectively. No significant peaks above the 0.1% FAP threshold remain in the residual periodogram after subtracting the main signal.

The spectral window function is shown in panel 3. GLS periodograms of the CCF FWHM (panel 4) and BIS (panel 5) are also shown; these diagnostics quantify line asymmetries that can mimic Doppler shifts and typically serve as indicators of stellar activity. There is no significant signals of the stellar activity in the periodogram is present. Although the CCF FWHM shows a peak coinciding with the spectral window function, it is therefore not considered significant.

3.5 Global Fit with EXOFASTv2

We used EXOFASTv2 (Eastman et al. 2019, hereafter EF2) to determine both the stellar and planetary parameters of the TOI-6884 system. EF2 is an exoplanet-fitting package written in IDL that can simultaneously model both RV and transit data. Additionally, it provides stellar parameters by fitting the spectral energy distribution (SED; Stassun & Torres 2016) and using MIST stellar evolutionary models (Choi et al. 2016; Dotter 2016). The EF2 package utilizes the Markov Chain Monte Carlo (MCMC) algorithm, and convergence is achieved when the Gelman-Rubin statistic is less than 1.01 and the number of independent draws exceeds 1000 (Gelman & Rubin 1992; Ford 2006).

The combination of SED, isochrones, and transit data allows a precise determination of the stellar mass, radius, and surface gravity (Torres et al. 2008). While fitting the RV and transit datasets and modelling the system, we applied Gaussian priors $[\text{Fe}/\text{H}]$ based on the spectroscopic parameters, and on the parallax derived from *Gaia* DR3 (Gaia Collaboration et al. 2023) after applying systematic corrections following Lindegren et al. (2021). Starting values of T_{eff} and $\log g$ were also provided. For SED fitting, we used photometric magnitudes from the *Gaia* G , G_{BP} , and G_{RP} bands, along with the 2MASS J , H , and K_S bands, and the WISE $W1$, $W2$, and $W3$ bands, as listed in Table 3. To account for systematic errors in the absolute photometry, the uncertainties in these magnitudes were inflated following the method outlined in Lindegren et al. (2021). Additionally, we applied a uniform prior to enforce an upper limit on the V-band extinction, using the Schlafly & Finkbeiner (2011) dust maps at the location of TOI-6884.

We performed a global model fit with EF2, keeping the eccentricity as a free parameter. In the process, we also provided the initial values for the orbital period (P) and central transit time (T_C), which were taken from the ExoFOP website. The priors are listed in Table A1. A Keplerian orbit is fitted for the RV, while the transit model is created using the approach of Mandel & Agol (2002) and Agol et al. (2020), with limb-darkening parameters constrained by Claret & Bloemen (2011) and Claret (2017). The EF2 fits revealed slight bimodality in the posterior distributions of stellar mass and age. This bimodality is not unprecedented; it is a known feature in certain regions of the MIST models (e.g. Khandelwal et al. 2022; Baliwal et al. 2024; Baliwal et al. 2025). The two peaks in mass are found at 1.21 and $1.41 M_{\odot}$. We split the distribution at the local minimum of $1.27 M_{\odot}$ and extracted both solutions, ultimately adopting the high-mass solution due to its higher relative probability (77%). All reported parameters and subsequent analyses are based on this solution.

The best-fit Kurucz stellar atmosphere model from the SED and the best-fit MIST stellar evolutionary model are shown in Fig. 9 and Fig. 10, respectively. We find that the host star is a late F-type slightly evolved star with parameters $M_* = 1.410^{+0.075}_{-0.069} M_{\odot}$, $R_* = 1.840^{+0.072}_{-0.073} R_{\odot}$, $T_{\text{eff}} = 6330^{+180}_{-160}$ K, $\log g = 4.057^{+0.045}_{-0.039}$, and an age of $2.61^{+0.78}_{-0.75}$ Gyr. These parameters are consistent with those derived from spectral synthesis in Sec. 3.1. The best-fit transit light curve and RV models are shown in Fig. 1, 3 and Fig. 8, respectively. Joint modeling reveals a BD companion with a radius $R_p = 0.927^{+0.051}_{-0.052} R_J$ and a mass $M_p = 26.32^{+0.98}_{-0.93} M_J$ in a nearly circular orbit $e = 0.067^{+0.010}_{-0.012}$ with an orbital period of $P = 4.808264^{+0.000015}_{-0.000014}$ days. We also calculate a Lucy–Sweeney probability (Lucy & Sweeney 1971) of $2.96 \times 10^{-5}\%$, confirming that the measured eccentricity is highly significant and not spurious. The best-fit stellar and planetary parameters, along with their 68% confidence intervals for the high-mass solution and low mass solutions, are listed in Table A1 and A2.

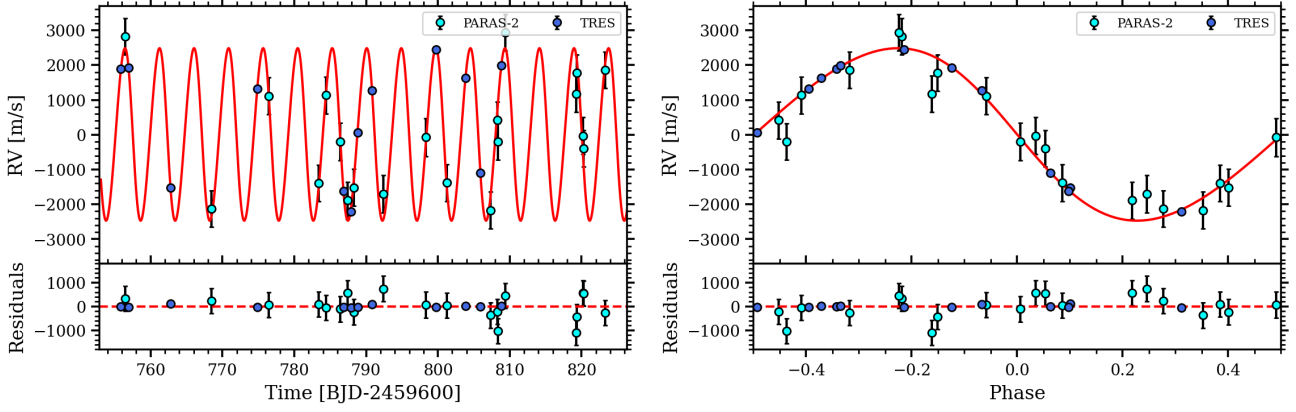


Figure 8. RV measurements of TOI-6884 from PARAS-2 (cyan points) and TRES (blue points) are shown as a function of time (left panel). The phase-folded RVs are shown in the right panel. The red line represents the best-fit RV model using EF2, with the residuals displayed in the lower panels.

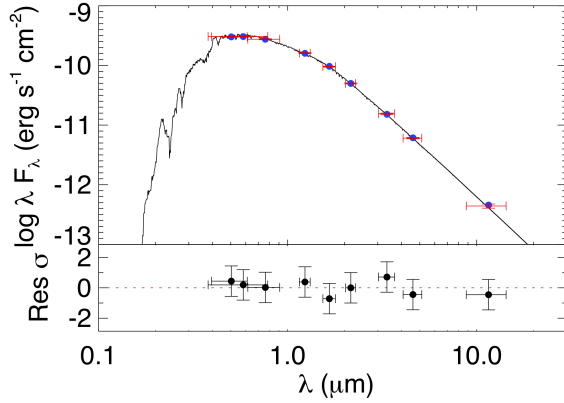


Figure 9. SED of TOI-6884, with red symbols representing the observed photometric measurements and horizontal bars indicating the effective width of the passbands. The blue points represent the model fluxes, and the residuals are displayed in the lower panel.

4 DISCUSSION

4.1 The transiting BD population and the Mass–Radius relation

We compiled a comparison sample of transiting BDs and gathered their properties from the TEPcat catalogue (Southworth 2011, and references therein). For this discussion, we define a brown dwarf as a substellar object with a mass between $13 M_J$ and $80 M_J$. There are a total of 49 transiting BDs in the sample and TOI-6884b adds one new member to this population, with a precisely determined mass and radius (i.e., with $<10\%$ uncertainties). Fig. 11 presents the mass–radius ($M - R$) distribution for these systems, including TOI-6884b. The BDs are color-coded by the ages of their host stars, and we overplot evolutionary models isochrones from the Sonora Diamondback grid (S24; Morley et al. 2024), using the same color coding as the BD sample. We chose the S24 models because they account for the effects of both clouds and metallicity. In particular, we adopt the ‘hybrid’ case where clouds are included above 1300 K and cloud-free below 1300 K. We show substellar models for ages of 0.11 Gyr, 0.49 Gyr, 1 Gyr, 2.5 Gyr, 5.3 Gyr, and 9.7 Gyr in the figure. To explore metallicity effects, we also include the 2.5 Gyr isochrone for $[M/H]$ of -0.5 and $+0.5$.

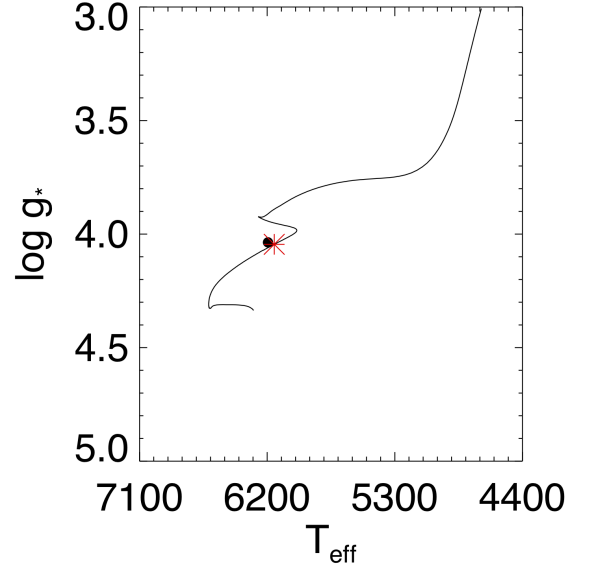


Figure 10. MIST evolutionary track for TOI-6884 shown as a solid black line. The black point indicates the T_{eff} and $\log g$, while the red asterisk denotes the current age of TOI-6884

Our analysis yields a mass and radius for TOI-6884b of $26.32^{+0.98}_{-0.93} M_J$ and $0.927^{+0.051}_{-0.052} R_J$, respectively. The stellar age derived from MIST isochrones shows a bimodal solution of either 2.61 or 5.19 Gyr, with respective probabilities of 0.77 and 0.23. As shown in Figure 11, TOI-6884b lies between the 1 Gyr and 9.7 Gyr isochrones, consistent with an age in the 2.6–5.2 Gyr range indicated by both the S24 and MIST models. This agreement remains robust even when accounting for metallicity variations, reinforcing the reliability of the inferred age.

Moreover, to investigate how incident stellar flux influences the radii of hot Jupiters, BDs, and low-mass stars, Lin et al. (2023) derived a flux–radius power-law relation for BDs and low-mass stars, analogous to the relation previously obtained by Weiss et al. (2013) for hot Jupiters. Their analysis yielded an empirical flux–radius rela-

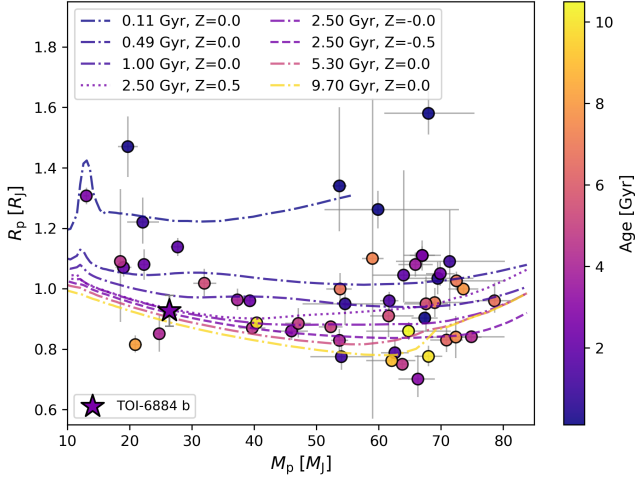


Figure 11. $M - R$ diagram of all known transiting BDs with masses between $13 M_J$ and $80 M_J$. TOI-6884b is marked with a star. Points are color-coded by the published ages of their host systems. Colored lines show evolutionary isochrones from Morley et al. (2024) at ages of 0.11, 0.49, 1.0, 2.5, 5.2, and 9.3 Gyr. Different line styles indicate metallicity variations ($[M/H] = -0.5, 0.0, +0.5$) for the 2.5 Gyr isochrone.

tion for BDs in the mass range $13-80 M_J$:

$$\frac{R_p}{R_J} = 1.11 \left(\frac{M_p}{M_J} \right)^{-0.052} \left(\frac{F}{F_\oplus} \right)^{0.009}. \quad (1)$$

For TOI-6884b, the predicted radius from this relation, $R_p = 0.998 R_J$ (Equation 1), agrees well within uncertainties with our radius measurement, showing no evidence of radius inflation. We also consider the substellar evolutionary models of Mukherjee et al. (2025), which explicitly incorporate the effects of incident stellar flux (expressed as $\log F$) on the radii of irradiated brown dwarfs as a function of mass and age. These models predict that strong irradiation (e.g., $\log_{10}(F/\text{cgs}) \geq 9$, corresponding to $T_{\text{eq}} \geq 1450$ K) can lead to radius enhancement, particularly at younger ages. TOI-6884b receives an incident flux of $1.68^{+0.14}_{-0.13} \times 10^9$ cgs, placing it within this irradiated regime. However, Mukherjee et al. (2025) also show that the impact of irradiation on brown dwarf radii decreases significantly at Gyr timescales (see Fig. 4; Mukherjee et al. 2025). In this context, the radius of TOI-6884b remains consistent with the empirical flux–radius relation of Lin et al. (2023), suggesting no strong evidence for anomalous inflation. This interpretation is further supported by theoretical studies on giant planets (e.g., Burrows et al. 2007), which indicate that the effect of stellar irradiation on planet radii diminishes with increasing object mass at an age of ~ 2.5 Gyr. These comparisons suggest that TOI-6884b does not exhibit significant radius inflation despite its relatively high incident flux, consistent with earlier suggestions that irradiation has a weaker impact on brown dwarfs than on hot Jupiters (Bouchy et al. 2011). Nevertheless, the non-zero flux dependence in the Lin et al. (2023) relation indicates that irradiation effects may not be entirely negligible (e.g., Page et al. 2024; Psaridi et al. 2022). A larger and uniformly characterized sample of transiting BDs will be essential to better constrain the role of irradiation in shaping their radii.

4.2 Tidal evolution

Given the small orbital separation of the TOI-6884 system, tidal effects play a dominant role in its orbital evolution and circularisation.

At present, there is no clear understanding of how to determine tidal quality factors for a system without detailed knowledge of the composition of the bodies (e.g., Jackson et al. 2008). Therefore, we adopt a broad range of tidal quality factor values from the literature and estimate the circularisation timescales using the equations described in Jackson et al. (2009) and their approximations as discussed in Henderson et al. (2024):

$$\frac{1}{a} \frac{da}{dt} = - \left[\frac{63}{2} \left(\frac{R_p^5 \sqrt{GM_\star^3}}{Q'_p M_p} \right) e^2 + \frac{9}{2} \sqrt{\frac{G}{M_\star}} \frac{R_\star^5 M_p}{Q'_\star} \left(1 + \frac{57}{4} e^2 \right) \right] a^{-\frac{13}{2}} \quad (2)$$

$$\frac{1}{e} \frac{de}{dt} = - \left[\frac{63}{4} \sqrt{GM_\star^3} \left(\frac{R_p^5}{Q'_p M_p} \right) + \frac{225}{16} \sqrt{\frac{G}{M_\star}} \left(\frac{R_\star^5 M_p}{Q'_\star} \right) \right] a^{-\frac{13}{2}} \quad (3)$$

The results are summarized in Table 4. In planetary systems, the effects of stellar tides (represented by Q'_\star) are often neglected compared to planetary tides (represented by Q'_p) because of the small mass ratios. This approximation can be considered to provide an upper limit on the circularisation timescales. Given the nearly circularized orbit of TOI-6884b ($e \sim 0.06$) and the age of the system (≈ 2.61 Gyr), we can put the constraints $Q'_p \geq 10^5$ and $Q'_\star \leq 10^{7.5}$, purely based on the argument that the system’s circularisation should happen within its lifetime (see Table 4). These estimates are also in broad agreement with other conservative estimates adopted in the literature (Lanza et al. 2011; Beatty et al. 2018).

The prescription used above inherently assumes that the variation in the semi-major axis is negligible as the circularisation happens. This need not be the case if stellar tides are significant for a system (Jackson et al. 2008). Therefore, in order to evaluate the impact of stellar tides on these estimates, we performed a complete numerical integration of equations 2 and 3 over a forward and backward period of 10 Gyr. It should be noted that higher order effects start coming up for $a \geq 0.2$ AU in which case the validity of the equations 2 and 3 becomes uncertain (see discussion in Jackson et al. (2008, 2009)). We considered different values of Q'_p for specific representative values of Q'_\star to assess their effect on the eccentricity evolution of the system and the results are presented in Fig. 12 and A2. It is evident that stronger stellar tides lead to faster circularisation (dash-dotted curves compared to solid ones). This behaviour seems to be in broad agreement with the conservative approach used to calculate the approximate circularisation timescales, thereby putting more confidence on the tidal parameter constraints derived therein.

We estimated the tidal synchronization timescales following the formalism of Albrecht et al. (2012), obtaining $\tau_{\text{CE}} = 1.36^{+0.35}_{-0.33}$ Gyr and $\tau_{\text{RA}} = 2.55^{+0.91}_{-0.78} \times 10^4$ Gyr. Here, τ_{CE} corresponds to stars with convective envelopes (typically $T_{\text{eff}} \leq 6250$ K), while τ_{RA} applies to stars with radiative envelopes ($T_{\text{eff}} \geq 6250$ K), where tidal dissipation is significantly less efficient. The transition between these two regimes occurs near the Kraft break (Kraft 1967), at $T_{\text{eff}} \sim 6250$ K, marking a change in both tidal dissipation efficiency and magnetic braking. With an effective temperature of $T_{\text{eff}} = 6330^{+180}_{-160}$ K, the host star lies close to this boundary. If the star possesses a radiative envelope, the synchronization timescale greatly exceeds the system age, implying inefficient tidal synchronization. In contrast, assuming a convective envelope yields a timescale shorter than the system age, suggesting that the system should be tidally synchronized. However, the observed stellar rotation period, $P_{\text{rot}} = 6.89 \pm 0.05$ d, differs from the orbital period, $P_{\text{orb}} = 4.808$ d, indicating that the system is not synchronized. This behavior is more consistent with the

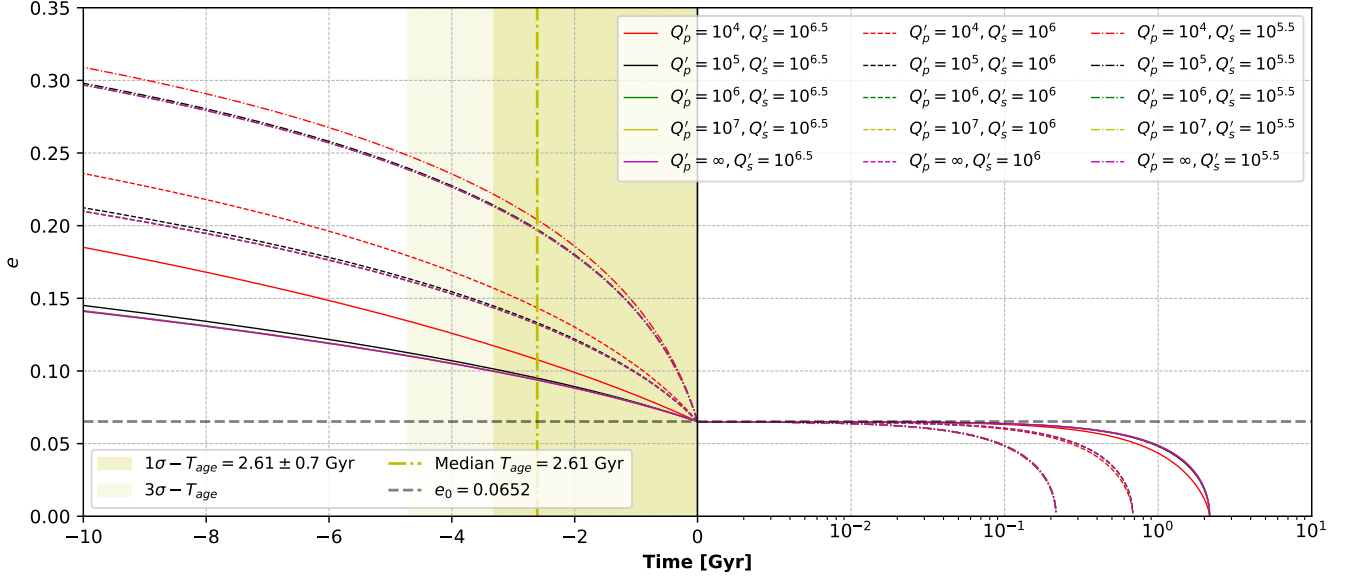


Figure 12. Backward and forward evolution of the orbital separation for different values of Q'_\star and Q'_p , based on the formulation of [Jackson et al. \(2009\)](#), for the high-probability solution of the TOI-6884 system. The low-probability solution is shown in Fig A2.

radiative-envelope regime and suggests inefficient tidal dissipation. The discrepancy between theoretical expectations and observations may reflect uncertainties in tidal dissipation mechanisms, making this system a compelling target for further investigation.

4.3 Eccentricity distribution

The orbital period and eccentricity together provide valuable insights into the dynamical evolution of transiting systems. As discussed in Section 4.2, the low eccentricity of TOI-6884b is consistent with its relatively short tidal circularisation timescale. The low eccentricity of TOI-6884 b ($e = 0.067^{+0.010}_{-0.012}$) is consistent with the “planet-like” distribution often observed for BDs below $42.5 M_J$ ([Ma & Ge 2014](#)). Though this behavioral transition remains a subject of debate ([Vowell et al. 2025](#)).

Moreover, in the context of giant planets, [Grunblatt et al. \(2018\)](#) found that those orbiting evolved stars, primarily red giant branch (RGB) hosts, tend to exhibit higher eccentricities (median $e \approx 0.152$) than planets around main-sequence hosts (median $e \approx 0.056$). This trend has been attributed to enhanced tidal interactions as stellar radii expand during post-main-sequence evolution. However, such systems are not directly comparable to subgiant hosts, which have not yet undergone the substantial radius expansion characteristic of red giants. In these systems, planets with shorter tidal circularisation timescales are expected to undergo rapid orbital decay and eventual engulfment, leaving behind a population dominated by high-eccentricity systems. Extending this trend to BDs orbiting subgiant stars is therefore not straightforward. In addition, the higher masses of BDs compared to giant planets can lead to stronger tidal interactions and shorter circularisation timescales, potentially altering their orbital evolution. In this context, TOI-6884b exhibits a relatively low eccentricity ($e = 0.067^{+0.010}_{-0.012}$), which may be consistent with efficient tidal circularisation. Currently, only 11 BDs have been detected around evolved stars, including TOI-6884b. Among these, only two, TOI-5882b ([Vowell et al. 2025](#)) and TOI-1994b ([Page et al. 2024](#)), fall within the low-mass regime and have masses comparable to TOI-6884b. Given the limited sample size, it remains unclear whether the

orbital architectures of BDs around evolved stars systematically differ from those of planets around main-sequence or red giant hosts.

4.4 Future work

TOI-6884 b presents several opportunities for future follow-up, particularly in the context of atmospheric characterisation and orbital architecture. Using the framework of [Kempton et al. \(2018\)](#), we estimate the transmission spectroscopy metric (TSM) and emission spectroscopy metric (ESM) for this system. The derived TSM value of ~ 0.9 indicates that the object is not a favourable target for transmission spectroscopy. We note, however, that the TSM formalism was primarily developed for smaller exoplanets, and its applicability to objects in the BD regime is uncertain. Similarly, the ESM metric of [Kempton et al. \(2018\)](#) was formulated for irradiated exoplanets and does not explicitly account for the intrinsic thermal emission of a BD. As a result, our estimated ESM value of ~ 16 should be regarded as a lower limit, since the BD’s own emission is expected to further enhance the planet-to-star flux contrast at infrared wavelengths. Even under this conservative assumption, the estimated ESM exceeds the threshold value of 7.5 suggested by [Kempton et al. \(2018\)](#), indicating that TOI-6884 b is a promising target for atmospheric characterisation via emission spectroscopy. The system is therefore well suited for detailed atmospheric studies with current and upcoming facilities such as the *James Webb Space Telescope* (JWST; [Gardner et al. 2006](#)) and *ARIEL* ([Tinetti et al. 2022](#)).

Beyond atmospheric studies, TOI-6884 b is also a promising target for investigating its orbital configuration via the Rossiter–McLaughlin (RM; [Triaud 2018](#)) effect, which provides a robust measurement of the sky-projected obliquity of the system. If the inclination of the stellar spin axis is known, this measurement can be used to infer the true stellar obliquity. As discussed in Section 3.2, TOI-6884 b is likely to be aligned based on our estimate of the stellar inclination angle; however, the system obliquity remains unconstrained. The expected RM semi-amplitude of $\sim 33 \text{ m s}^{-1}$ is well within the capabilities of current high-resolution spectrographs, enabling detection and modelling of the RM anomaly during transit.

Table 4. Tidal circularisation timescales for the TOI-6884 system estimated using approximations to tidal evolution equations (Jackson et al. 2008, 2009) for both high and low probability mass solutions derived from EF2.

Q'_*	Q'_p	$\tau_{\text{circ}}^{\text{eff}}$ (Gyr)	
		High-probability	Low-probability
10^5	$10^{4.5}$	0.02	0.02
	10^5	0.02	0.02
	$10^{5.5}$	0.02	0.02
	10^6	0.02	0.02
	$10^{6.5}$	0.02	0.02
$10^{5.5}$	$10^{4.5}$	0.07	0.05
	10^5	0.07	0.05
	$10^{5.5}$	0.07	0.05
	10^6	0.07	0.05
	$10^{6.5}$	0.07	0.05
10^6	$10^{4.5}$	0.23	0.16
	10^5	0.23	0.16
	$10^{5.5}$	0.24	0.16
	10^6	0.24	0.16
	$10^{6.5}$	0.24	0.16
10^7	$10^{4.5}$	1.60	1.10
	10^5	2.05	1.42
	$10^{5.5}$	2.26	1.56
	10^6	2.33	1.61
	$10^{6.5}$	2.36	1.62
$10^{7.5}$	$10^{4.5}$	2.96	2.05
	10^5	5.04	3.48
	$10^{5.5}$	6.49	4.48
	10^6	7.14	4.92
	$10^{6.5}$	7.37	5.08
$Q'_* \rightarrow \infty$	$10^{4.5}$	4.89	3.39
	10^5	15.46	10.71
	$10^{5.5}$	48.90	33.88
	10^6	154.63	107.14
	$10^{6.5}$	488.98	338.80

Such observations would yield a direct measurement of the spin-orbit angle, λ , providing valuable constraints on the formation and dynamical evolution of this close-in brown dwarf. Combined atmospheric and RM observations would therefore offer a more complete picture of the physical and dynamical properties of the TOI-6884 system.

5 SUMMARY

In this work, we report the discovery and characterisation of TOI-6884 b, a transiting BD orbiting a slightly evolved F-type star. The system was initially identified as an exoplanet candidate from transit signals detected by NASA's *TESS* mission with a reported orbital period of ~ 14.42 days. Through careful re-analysis of the *TESS* photometry and confirmation with ground-based follow-up observations, we identified the true orbital period to be $4.808264^{+0.000015}_{-0.000014}$ days, corresponding to a one-third harmonic of the initially reported value. The substellar nature of the companion was confirmed through ex-

tensive follow-up, including high-precision radial velocity measurements with PARAS-2 at the PRL 2.5 m telescope and TRES at FLWO, time-series transit photometry obtained with TCS/MuSCAT-2, LCO/Teide, LCO/McDonald, and LCO-HAL/MuSCAT-3, as well as high-angular-resolution imaging from Gemini, WIYN, and SAI, which rule out close stellar companions. From a joint analysis of the photometric and spectroscopic data, we determine that the host star is an F-type star with an effective temperature of 6330^{+180}_{-160} K, a metallicity of $[\text{Fe}/\text{H}] = 0.094^{+0.073}_{-0.068}$, and stellar parameters consistent with a slightly evolved star. The derived stellar mass, radius, and age are $1.410^{+0.075}_{-0.069} M_{\odot}$, $1.840^{+0.072}_{-0.073} R_{\odot}$, and $2.61^{+0.78}_{-0.75}$ Gyr, respectively. The companion, TOI-6884 b, has a mass of $26.32^{+0.98}_{-0.93} M_{\text{J}}$ and a radius of $0.927^{+0.051}_{-0.052} R_{\text{J}}$, placing it securely in the BD regime. Its orbit exhibits a small but non-zero eccentricity of $0.067^{+0.010}_{-0.012}$, and the estimated equilibrium temperature is 1652 ± 32 K. TOI-6884 b adds to the small but growing sample of well-characterised transiting BDs, particularly in the regime of short orbital periods around slightly evolved, late-type host stars. Such systems provide important empirical constraints on the mass–radius relation and orbital properties of substellar companions, and contribute to improving our understanding of BD structure and evolution across different irradiation and tidal environments.

ACKNOWLEDGEMENTS

We acknowledge the PRL-DOS (Department of Space, Government of India) and the director of PRL for supporting the PARAS spectrograph funding for the exoplanet discovery project and the research grant for AK, SB, and SD. We also acknowledge support from the Swiss National Science Foundation IZSTZ0_216537 and the Centre for Space and Habitability (CSH) of the University of Bern. Part of this work received support from the National Centre for Competence in Research PlanetS, supported by the Swiss National Science Foundation (SNSF). YGMC, MPM, SP, and AK are partially supported by UNAM PAPIIT-IG101224. The work of B.S. and P.B. was conducted under the state assignment of Lomonosov Moscow State University. Participation of KN was made possible by the SETI Institute REU internship program (NSF award 2051007). This work makes use of observations from the LCOGT network. Part of the LCOGT telescope time was granted by NOIRLab through the Mid-Scale Innovations Program (MSIP). MSIP is funded by NSF. This paper is based on observations made with the Las Cumbres Observatory's education network telescopes that were upgraded through generous support from the Gordon and Betty Moore Foundation. This article is based on observations made with the MuSCAT2 instrument, developed by ABC, at Telescopio Carlos Sánchez operated on the island of Tenerife by the IAC in the Spanish Observatorio del Teide. This paper is based on observations made with the MuSCAT3 instrument, developed by the Astrobiology Center and under financial supports by JSPS KAKENHI (JP18H05439) and JST PRESTO (JPMJPR1775), at Faulkes Telescope North on Maui, HI, operated by the Las Cumbres Observatory. This work is partly supported by JSPS KAKENHI Grant Numbers JP24H00017, JP24K00689, JSPS Bilateral Program Number JPJSBP120249910 and JSPS Grant-in-Aid for JSPS Fellows Grant Number JP25KJ0091. This work is partly financed by the Spanish Ministry of Economics and Competitiveness through grants PGC2018-098153-B-C31. This research has made use of the Exoplanet Follow-up Observation Program (ExoFOP; DOI: 10.26134/ExoFOP5) website, which is operated by the California Institute of Technology, under contract with the National

Aeronautics and Space Administration under the Exoplanet Exploration Program. Funding for the TESS mission is provided by NASA's Science Mission Directorate. KAC and CNW acknowledge support from the TESS mission via subaward s3449 from MIT. Some of the observations in this paper made use of the High-Resolution Imaging instrument 'Alopeke and were obtained under Gemini LLP Proposal Number: GN/S-2021A-LP-105. 'Alopeke was funded by the NASA Exoplanet Exploration Program and built at the NASA Ames Research Center by Steve B. Howell, Nic Scott, Elliott P. Horch, and Emmett Quigley. Alopeke was mounted on the Gemini North telescope of the international Gemini Observatory, a program of NSF's OIR Lab, which is managed by the Association of Universities for Research in Astronomy (AURA) under a cooperative agreement with the National Science Foundation, on behalf of the Gemini partnership: the National Science Foundation (United States), National Research Council (Canada), Agencia Nacional de Investigación y Desarrollo (Chile), Ministerio de Ciencia, Tecnología e Innovación (Argentina), Ministério da Ciência, Tecnologia, Inovações e Comunicações (Brazil), and Korea Astronomy and Space Science Institute (Republic of Korea). We acknowledge financial support from the Agencia Estatal de Investigación of the Ministerio de Ciencia e Innovación MCIN/AEI/10.13039/501100011033 and the ERDF "A way of making Europe" through projects PID2021-125627OB-C32 and PID2024-158486OB-C32. We thank the anonymous referee for careful reading of this manuscript and useful suggestions.

DATA AVAILABILITY

The *TESS* photometric data and the high-resolution speckle imaging observations used in this work are publicly available through the Mikulski Archive for Space Telescopes (MAST; <https://mast.stsci.edu/>) and the ExoFOP-*TESS* portal (<https://exofop.ipac.caltech.edu/tess/target.php?id=156514476>), respectively. The ground-based photometric follow-up data are also available on the ExoFOP-*TESS* page. The radial velocity measurements underlying this article are provided in Table 2. All other data supporting the findings of this study will be shared by the corresponding author upon reasonable request.

REFERENCES

- Adams F. C., Laughlin G., 2006, *ApJ*, **649**, 1004
- Agol E., Luger R., Foreman-Mackey D., 2020, *The Astronomical Journal*, **159**, 123
- Albrecht S., et al., 2012, *ApJ*, **757**, 18
- Alibert Y., Mordasini C., Benz W., Winisdoerffer C., 2005, *A&A*, **434**, 343
- Aller A., Lillo-Box J., Jones D., Miranda L. F., Barceló Forteza S., 2020, *A&A*, **635**, A128
- Baliwal S., et al., 2024, *A&A*, **691**, A12
- Baliwal S., et al., 2025, *AJ*, **169**, 147
- Baraffe I., Chabrier G., Allard F., Hauschildt P. H., 2002, *A&A*, **382**, 563
- Baraffe I., Homeier D., Allard F., Chabrier G., 2015, *A&A*, **577**, A42
- Baranne A., et al., 1996, *A&AS*, **119**, 373
- Barragán O., Aigrain S., Rajpaul V. M., Zicher N., 2021, *Monthly Notices of the Royal Astronomical Society*, **509**, 866
- Beatty T. G., Morley C. V., Curtis J. L., Burrows A., Davenport J. R. A., Montet B. T., 2018, *AJ*, **156**, 168
- Bensby T., Feltzing S., Oey M. S., 2014, *A&A*, **562**, A71
- Bouchy F., et al., 2011, *A&A*, **525**, A68
- Brown T. M., et al., 2013, *PASP*, **125**, 1031
- Buchhave L. A., et al., 2010, *ApJ*, **720**, 1118
- Buchhave L. A., et al., 2012, *Nature*, **486**, 375
- Burrows A., Hubeny I., Budaj J., Hubbard W. B., 2007, *ApJ*, **661**, 502
- Burrows A., Heng K., Nampaisarn T., 2011, *ApJ*, **736**, 47
- Butters O. W., et al., 2010, *A&A*, **520**, L10
- Castro-González A., et al., 2024, *A&A*, **691**, A233
- Chabrier G., Baraffe I., Allard F., Hauschildt P., 2000, *ApJ*, **542**, 464
- Chabrier G., Baraffe I., Phillips M., Debras F., 2023, *A&A*, **671**, A119
- Chakraborty A., Thapa N., Kumar K., Neelam P. J. S. S. V., Sharma R., Roy A., 2018, in Evans C. J., Simard L., Takami H., eds, *Society of Photo-Optical Instrumentation Engineers (SPIE) Conference Series Vol. 10702, Ground-based and Airborne Instrumentation for Astronomy VII*. p. 107026G, doi:10.1117/12.2313055
- Chakraborty A., et al., 2024, *Bulletin de la Société Royale des Sciences de Liège*, p. 68–88
- Chaturvedi P., Chakraborty A., Anandarao B. G., Roy A., Mahadevan S., 2016, *Monthly Notices of the Royal Astronomical Society*, **462**, 554
- Choi J., Dotter A., Conroy C., Cantiello M., Paxton B., Johnson B. D., 2016, *ApJ*, **823**, 102
- Ciardi D. R., Beichman C. A., Horch E. P., Howell S. B., 2015, *ApJ*, **805**, 16
- Claret A., 2017, *A&A*, **600**, A30
- Claret A., Bloemen S., 2011, *A&A*, **529**, A75
- Collins K. A., Kielkopf J. F., Stassun K. G., Hessman F. V., 2017, *AJ*, **153**, 77
- Cutri R. M., et al., 2003, *VizieR Online Data Catalog*, p. II/246
- Cutri R. M., et al., 2021, *VizieR Online Data Catalog*, p. II/328
- Dekany R., et al., 2013, *ApJ*, **776**, 130
- Dotter A., 2016, *ApJS*, **222**, 8
- Eastman J. D., et al., 2019, arXiv e-prints, p. arXiv:1907.09480
- Fűrész G., 2008, PhD thesis, University of Szeged, Hungary
- Ford E. B., 2006, *ApJ*, **642**, 505
- Furlan E., Howell S. B., 2017, *AJ*, **154**, 66
- Furlan E., Howell S. B., 2020, *ApJ*, **898**, 47
- Furlan E., et al., 2017, *AJ*, **153**, 71
- Gagné J., et al., 2018, *ApJ*, **856**, 23
- Gaia Collaboration et al., 2023, *A&A*, **674**, A1
- Gardner J. P., et al., 2006, *Space Sci. Rev.*, **123**, 485
- Gelman A., Rubin D. B., 1992, *Statistical Science*, **7**, 457
- Grievies N., et al., 2017, *MNRAS*, **467**, 4264
- Grievies N., et al., 2021, *A&A*, **652**, A127
- Grunblatt S. K., et al., 2016, *AJ*, **152**, 185
- Grunblatt S. K., et al., 2018, *ApJ*, **861**, L5
- Guerrero N. M., et al., 2021, *ApJS*, **254**, 39
- Halbwachs J. L., Mayor M., Udry S., Arenou F., 2003, *A&A*, **397**, 159
- Hayward T. L., Brandl B., Pirger B., Blacken C., Gull G. E., Schoenwald J., Houck J. R., 2001, *PASP*, **113**, 105
- Henderson B. A., et al., 2024, *MNRAS*, **533**, 2823
- Hennebelle P., Chabrier G., 2008, *ApJ*, **684**, 395
- Høg E., et al., 2000, *A&A*, **355**, L27
- Howell S. B., Everett M. E., Sherry W., Horch E., Ciardi D. R., 2011, *AJ*, **142**, 19
- Howell S. B., Scott N. J., Matson R. A., Everett M. E., Furlan E., Gnilka C. L., Ciardi D. R., Lester K. V., 2021, *Frontiers in Astronomy and Space Sciences*, **8**, 10
- Hut P., 1981, *A&A*, **99**, 126
- Jackson B., Greenberg R., Barnes R., 2008, *ApJ*, **678**, 1396
- Jackson B., Barnes R., Greenberg R., 2009, *ApJ*, **698**, 1357
- Jenkins J., et al., 2016, in *Software and Cyber infrastructure for Astronomy IV*, doi:10.1117/12.2233418
- Jensen E., 2013, Tapir: A web interface for transit/eclipse observability, Astrophysics Source Code Library (ascl:1306.007)
- Kempton E. M.-R., et al., 2018, *PASP*, **130**, 114401
- Khandelwal A., et al., 2022, *MNRAS*, **509**, 3339
- Kiefer F., Hébrard G., Lecavelier des Etangs A., Martioli E., Dalal S., Vidal-Madjar A., 2021, *A&A*, **645**, A7
- Kraft R. P., 1967, *ApJ*, **150**, 551
- Kratter K., Lodato G., 2016, *ARA&A*, **54**, 271
- Kreidberg L., 2015, *Publications of the Astronomical Society of the Pacific*, **127**, 1161–1165

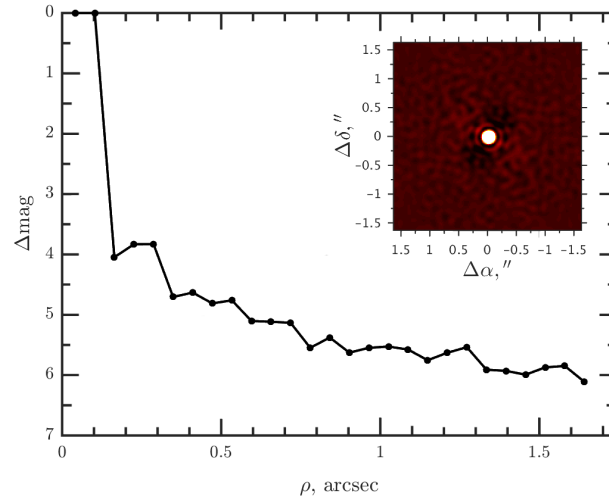
- Kurucz R. L., 1992, in Barbu B., Renzini A., eds, IAU Symposium Vol. 149, The Stellar Populations of Galaxies. p. 225
- Lanza A. F., Damiani C., Gandolfi D., 2011, *A&A*, 529, A50
- Leggett S. K., 1992, *ApJS*, 82, 351
- Lester K. V., et al., 2021, *AJ*, 162, 75
- Lillo-Box J., Barrado D., Bouy H., 2014, *A&A*, 566, A103
- Lin Z., et al., 2023, *MNRAS*, 523, 6162
- Lindgren et al., 2021, *A&A*, 649, A2
- Lucy L. B., Sweeney M. A., 1971, *AJ*, 76, 544
- Ma B., Ge J., 2014, *MNRAS*, 439, 2781
- Mandel K., Agol E., 2002, *ApJ*, 580, L171
- Masuda K., Winn J. N., 2020, *AJ*, 159, 81
- Matson R., Howell S., Horch E., Everett M., 2018, in American Astronomical Society Meeting Abstracts #231. p. 109.02
- McCully C., Volgenau N. H., Harbeck D.-R., Lister T. A., Saunders E. S., Turner M. L., Siiverd R. J., Bowman M., 2018, in Proc. SPIE. p. 107070K ([arXiv:1811.04163](https://arxiv.org/abs/1811.04163)), doi:10.1117/12.2314340
- Mordasini C., Alibert Y., Benz W., Naef D., 2009, *A&A*, 501, 1161
- Morley C. V., et al., 2024, *ApJ*, 975, 59
- Mukherjee S., Fortney J. J., Carmichael T. W., Davis C. E., Thorngren D. P., 2025, *arXiv e-prints*, p. [arXiv:2512.08249](https://arxiv.org/abs/2512.08249)
- Narita N., et al., 2019, *Journal of Astronomical Telescopes, Instruments, and Systems*, 5, 015001
- Narita N., et al., 2020, in Society of Photo-Optical Instrumentation Engineers (SPIE) Conference Series. p. 114475K, doi:10.1117/12.2559947
- Nguyen K. T., Caldwell D. A., Twicken J. D., Striegel S. L., Ting E. B., Williams R. H., Jenkins J. M., 2022, *Research Notes of the American Astronomical Society*, 6, 207
- Padoan P., Nordlund Å., 2004, *ApJ*, 617, 559
- Page E., et al., 2024, *AJ*, 167, 109
- Parviainen H., et al., 2019, *A&A*, 630, A89
- Phillips M. W., et al., 2020, *A&A*, 637, A38
- Psaridi A., et al., 2022, *A&A*, 664, A94
- Rodriguez J. E., et al., 2023, *MNRAS*, 521, 2765
- Saunders N., et al., 2022, *AJ*, 163, 53
- Schlafly E. F., Finkbeiner D. P., 2011, *ApJ*, 737, 103
- Schlaufman K. C., 2018, *ApJ*, 853, 37
- Schönrich R., Binney J., Dehnen W., 2010, *MNRAS*, 403, 1829
- Scott N. J., Howell S. B., Horch E. P., Everett M. E., 2018, *PASP*, 130, 054502
- Scott N. J., et al., 2021, *Frontiers in Astronomy and Space Sciences*, 8, 138
- Smith J. C., et al., 2012, *PASP*, 124, 1000
- Southworth J., 2011, *MNRAS*, 417, 2166
- Spiegel D. S., Burrows A., Milsom J. A., 2011, *ApJ*, 727, 57
- Stassun K. G., Torres G., 2016, *ApJ*, 831, L6
- Stassun K. G., et al., 2018, *AJ*, 156, 102
- Strakhov I. A., Safonov B. S., Cheryasov D. V., 2023, *Astrophysical Bulletin*, 78, 234
- Stumpe M. C., Smith J. C., Catanzarite J. H., Cleve J. E. V., Jenkins J. M., Twicken J. D., Girouard F. R., 2014, *Publications of the Astronomical Society of the Pacific*, 126, 100
- Tayar J., Stassun K. G., Corsaro E., 2019, *ApJ*, 883, 195
- Tinetti G., Eccleston P., Lueftinger T., Salvignol J.-C., Fahmy S., Alves de Oliveira C., 2022, in European Planetary Science Congress. pp EPSC2022–1114 ([arXiv:2104.04824](https://arxiv.org/abs/2104.04824)), doi:10.5194/epsc2022-1114
- Torres G., Winn J. N., Holman M. J., 2008, *ApJ*, 677, 1324
- Triaud A. H. M. J., 2018, in Deeg H. J., Belmonte J. A., eds, , Handbook of Exoplanets. p. 2, doi:10.1007/978-3-319-55333-7_2
- Veras D., 2016, *Royal Society Open Science*, 3, 150571
- Villaver E., Livio M., Mustill A. J., Siess L., 2014, *ApJ*, 794, 3
- Vowell N., et al., 2025, *AJ*, 170, 68
- Weiss L. M., et al., 2013, *ApJ*, 768, 14
- Yu J., Huber D., Bedding T. R., Stello D., 2018, *MNRAS*, 480, L48
- Zechmeister, M. Kürster, M. 2009, *A&A*, 496, 577

Table A1. Median values and 68% confidence interval for TOI-6884 for both the probability solutions.

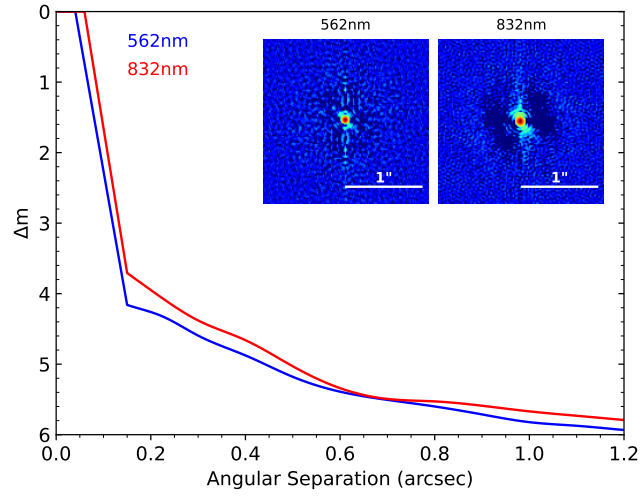
Parameter	Description	Value (Pr ~77%, high-mass)	Value (Pr ~23%, low-mass)
Stellar Parameters:			
M_*	Mass (M_\odot)	$1.410^{+0.075}_{-0.069}$	$1.212^{+0.035}_{-0.041}$
R_*	Radius (R_\odot)	$1.840^{+0.072}_{-0.073}$	$1.868^{+0.060}_{-0.061}$
L_*	Luminosity (L_\odot)	$4.91^{+0.45}_{-0.42}$	$4.57^{+0.39}_{-0.32}$
ρ_*	Density (cgs)	$0.318^{+0.048}_{-0.037}$	$0.261^{+0.026}_{-0.023}$
$\log g$	Surface gravity (cgs)	$4.057^{+0.045}_{-0.039}$	$3.977^{+0.028}_{-0.027}$
T_{eff}	Effective temperature (K)	6330^{+180}_{-160}	6180^{+140}_{-130}
[Fe/H]	Metallicity (dex)	$0.094^{+0.073}_{-0.068}$	$0.067^{+0.070}_{-0.061}$
Age	Age (Gyr)	$2.61^{+0.78}_{-0.75}$	$5.20^{+0.76}_{-0.55}$
EEP	Equal Evolutionary Phase	384^{+22}_{-29}	$448.3^{+5.2}_{-4.0}$
A_V	V-band extinction (mag)	$0.211^{+0.094}_{-0.098}$	$0.128^{+0.090}_{-0.081}$
σ_{SED}	SED photometry error scaling	$0.55^{+0.23}_{-0.14}$	$0.60^{+0.26}_{-0.16}$
ϖ	Parallax (mas)	1.778 ± 0.022	1.781 ± 0.022
d	Distance (pc)	$562.5^{+7.1}_{-7.0}$	$561.5^{+6.9}_{-6.8}$
Planetary Parameters:			
P , b	Period (days)	$4.808264^{+0.000015}_{-0.000014}$	$4.808264^{+0.000015}_{-0.000014}$
R_P , b	Radius (R_J)	$0.927^{+0.051}_{-0.052}$	$0.961^{+0.042}_{-0.043}$
M_P , b	Mass (M_J)	$26.32^{+0.98}_{-0.93}$	$23.84^{+0.54}_{-0.64}$
T_C , b	Observed Time of conjunction (BJD _{TDB})	$2459641.0987^{+0.0026}_{-0.0028}$	$2459641.0988^{+0.0026}_{-0.0029}$
a , b	Semi-major axis (AU)	$0.0629^{+0.0011}_{-0.0010}$	$0.05981^{+0.00057}_{-0.00067}$
i , b	Inclination (Degrees)	$82.46^{+0.45}_{-0.42}$	$81.80^{+0.34}_{-0.32}$
e , b	Eccentricity	$0.067^{+0.010}_{-0.012}$	$0.0684^{+0.0099}_{-0.011}$
ω_* , b	Arg of periastron (Degrees)	$82.3^{+5.2}_{-6.9}$	$82.7^{+4.9}_{-6.3}$
$\dot{\omega}_{GR,b}$	Computed GR precession ($^\circ$ /century)	$1.824^{+0.064}_{-0.060}$	$1.649^{+0.032}_{-0.037}$
$T_{\text{eq},b}$	Equilibrium temp (K)	1652 ± 32	1665^{+32}_{-28}
$\tau_{\text{circ},b}$	Tidal circ timescale (Gyr)	130^{+47}_{-32}	88^{+23}_{-17}
K , b	RV semi-amplitude (m/s)	2476^{+30}_{-34}	2476^{+30}_{-33}
R_P/R_* , b	Radius of planet in stellar radii	0.0517 ± 0.0011	0.05283 ± 0.00099
a/R_* , b	Semi-major axis in stellar radii	$7.34^{+0.35}_{-0.30}$	$6.87^{+0.22}_{-0.20}$
δ , b	$(R_P/R_*)^2$	$0.00268^{+0.00012}_{-0.00011}$	$0.00279^{+0.00011}_{-0.00010}$
$\delta_{g',b}$	Transit depth in g' (frac)	$0.002066^{+0.000086}_{-0.000092}$	$0.002011^{+0.000098}_{-0.00010}$
$\delta_{i',b}$	Transit depth in i' (frac)	$0.002403^{+0.000077}_{-0.000074}$	$0.002439^{+0.000077}_{-0.000076}$
$\delta_{r',b}$	Transit depth in r' (frac)	0.002235 ± 0.000076	$0.002224^{+0.000086}_{-0.000085}$
$\delta_{z',b}$	Transit depth in z' (frac)	$0.002432^{+0.000087}_{-0.000083}$	$0.002474^{+0.000090}_{-0.000087}$
$\delta_{TESS,b}$	Transit depth in TESS (frac)	$0.002369^{+0.000093}_{-0.000089}$	0.00239 ± 0.00010
τ , b	In/egress transit duration (days)	$0.0245^{+0.0032}_{-0.0030}$	$0.0291^{+0.0028}_{-0.0027}$
$T_{14,b}$	Total transit duration (days)	$0.1068^{+0.0022}_{-0.0021}$	0.1097 ± 0.0021
b , b	Transit impact parameter	$0.902^{+0.010}_{-0.013}$	$0.9150^{+0.0063}_{-0.0075}$
ρ_P , b	Density (cgs)	$41.0^{+8.2}_{-6.3}$	$33.2^{+4.9}_{-3.9}$
$\log g_P$, b	Surface gravity (cgs)	$4.880^{+0.055}_{-0.050}$	$4.805^{+0.040}_{-0.037}$
$\langle F \rangle$, b	Incident Flux ($10^9 \text{ erg s}^{-1} \text{ cm}^{-2}$)	$1.68^{+0.14}_{-0.13}$	$1.74^{+0.14}_{-0.11}$
$e \cos \omega_*$, b		$0.0089^{+0.0064}_{-0.0059}$	$0.0086^{+0.0063}_{-0.0058}$
$e \sin \omega_*$, b		$0.066^{+0.010}_{-0.013}$	$0.068^{+0.010}_{-0.012}$
$M_P \sin i$, b	Minimum mass (M_J)	$26.09^{+0.59}_{-0.93}$	$23.59^{+0.34}_{-0.64}$
M_P/M_* , b	Mass ratio	$0.01782^{+0.00039}_{-0.00041}$	$0.01880^{+0.00033}_{-0.00031}$
Wavelength Parameters:			
$u_{1,g'}$	Linear limb-darkening coeff	$0.440^{+0.042}_{-0.041}$	$0.458^{+0.041}_{-0.040}$
$u_{1,i'}$	Linear limb-darkening coeff	$0.222^{+0.027}_{-0.026}$	0.236 ± 0.025
$u_{1,r'}$	Linear limb-darkening coeff	$0.337^{+0.040}_{-0.039}$	0.355 ± 0.039
$u_{1,z'}$	Linear limb-darkening coeff	$0.200^{+0.039}_{-0.038}$	$0.214^{+0.038}_{-0.037}$
$u_{1,TESS}$	Linear limb-darkening coeff	0.245 ± 0.052	0.262 ± 0.050
$u_{2,g'}$	Quadratic limb-darkening coeff	0.254 ± 0.040	$0.234^{+0.038}_{-0.039}$
$u_{2,i'}$	Quadratic limb-darkening coeff	0.308 ± 0.021	0.302 ± 0.021
$u_{2,r'}$	Quadratic limb-darkening coeff	0.345 ± 0.035	0.339 ± 0.035
$u_{2,z'}$	Quadratic limb-darkening coeff	0.323 ± 0.035	0.319 ± 0.035
$u_{2,TESS}$	Quadratic limb-darkening coeff	0.320 ± 0.049	$0.317^{+0.048}_{-0.049}$

Table A2. Median values and 68% confidence interval for TOI-6884 for both the probability solutions.

Parameter	Description	Value (Pr ~77%, high-mass)	Value (Pr ~23%, low-mass)
Instrument Parameters:			
$\gamma_{\text{rel,PARAS}}$	Relative RV Offset (m/s)	-2350 ± 120	-2350 ± 120
$\gamma_{\text{rel,TRES}}$	Relative RV Offset (m/s)	-115 ± 23	-114 ± 22
σ_J, PARAS	RV Jitter (m/s)	520^{+110}_{-82}	522^{+110}_{-83}
σ_J, TRES	RV Jitter (m/s)	56^{+34}_{-22}	55^{+32}_{-21}
σ_J^2, PARAS	RV Jitter Variance	$271000^{+120000}_{-79000}$	$273000^{+130000}_{-80000}$
σ_J^2, TRES	RV Jitter Variance	3200^{+4900}_{-2000}	3100^{+4500}_{-1900}
Transit Parameters:			
$\sigma^2, \text{TESS UT 2022-03-14 (TESS)}$	Added Variance	$-0.000000068^{+0.000000026}_{-0.000000025}$	$-0.000000068^{+0.000000026}_{-0.000000025}$
$\sigma^2, \text{MuSCAT2 UT 2024-05-03 (g')}$	Added Variance	$-0.00002014^{+0.00000054}_{-0.00000051}$	$-0.00002015^{+0.00000054}_{-0.00000052}$
$\sigma^2, \text{MuSCAT2 UT 2024-05-03 (i')}$	Added Variance	$-0.00002014^{+0.00000053}_{-0.00000052}$	$-0.00002015^{+0.00000053}_{-0.00000051}$
$\sigma^2, \text{MuSCAT2 UT 2024-05-03 (r')}$	Added Variance	$0.00000099^{+0.00000039}_{-0.00000038}$	$0.00000099^{+0.00000040}_{-0.00000038}$
$\sigma^2, \text{MuSCAT2 UT 2024-05-03 (z')}$	Added Variance	$0.00000162^{+0.00000059}_{-0.00000056}$	$0.00000163^{+0.00000058}_{-0.00000056}$
$\sigma^2, \text{MuSCAT3 UT 2024-12-25 (g')}$	Added Variance	$0.00000093^{+0.00000016}_{-0.00000014}$	$0.00000093^{+0.00000015}_{-0.00000014}$
$\sigma^2, \text{MuSCAT3 UT 2024-12-25 (i')}$	Added Variance	$0.00000142^{+0.00000020}_{-0.00000018}$	$0.00000142^{+0.00000020}_{-0.00000018}$
$\sigma^2, \text{MuSCAT3 UT 2024-12-25 (r')}$	Added Variance	$0.00000193^{+0.00000019}_{-0.00000018}$	$0.00000192^{+0.00000019}_{-0.00000018}$
$\sigma^2, \text{MuSCAT3 UT 2024-12-25 (z')}$	Added Variance	$0.00000077^{+0.00000016}_{-0.00000014}$	$0.00000076^{+0.00000016}_{-0.00000014}$
$\sigma^2, \text{LCO UT 2460-35-2. (i')}$	Added Variance	$-0.00000112^{+0.00000079}_{-0.00000067}$	$-0.00000114^{+0.00000079}_{-0.00000066}$
$\sigma^2, \text{LCO UT 2460-40-5. (i')}$	Added Variance	$0.00000239^{+0.00000026}_{-0.00000024}$	$0.00000238^{+0.00000026}_{-0.00000024}$
$\sigma^2, \text{LCO UT 2460-42-4. (i')}$	Added Variance	$0.00000258^{+0.00000032}_{-0.00000030}$	$0.00000258^{+0.00000032}_{-0.00000030}$
$\sigma^2, \text{LCO UT 2460-42-9. (i')}$	Added Variance	$0.00000115^{+0.00000031}_{-0.00000027}$	$0.00000117^{+0.00000031}_{-0.00000028}$
$F_0, \text{TESS UT 2022-03-14 (TESS)}$	Baseline flux	1.00017 ± 0.000019	$1.000018^{+0.000018}_{-0.000019}$
$F_0, \text{MuSCAT2 UT 2024-05-03 (g')}$	Baseline flux	$1.000041^{+0.000089}_{-0.000088}$	$1.000044^{+0.000090}_{-0.000089}$
$F_0, \text{MuSCAT2 UT 2024-05-03 (i')}$	Baseline flux	1.000110 ± 0.000088	$1.000119^{+0.000089}_{-0.000088}$
$F_0, \text{MuSCAT2 UT 2024-05-03 (r')}$	Baseline flux	1.000146 ± 0.000081	1.000143 ± 0.000082
$F_0, \text{MuSCAT2 UT 2024-05-03 (z')}$	Baseline flux	1.000441 ± 0.000096	$1.000448^{+0.000098}_{-0.000097}$
$F_0, \text{MuSCAT3 UT 2024-12-25 (g')}$	Baseline flux	0.999690 ± 0.000089	$0.999694^{+0.000090}_{-0.000089}$
$F_0, \text{MuSCAT3 UT 2024-12-25 (i')}$	Baseline flux	0.999922 ± 0.000086	0.999936 ± 0.000086
$F_0, \text{MuSCAT3 UT 2024-12-25 (r')}$	Baseline flux	1.000070 ± 0.000082	$1.000066^{+0.000084}_{-0.000083}$
$F_0, \text{MuSCAT3 UT 2024-12-25 (z')}$	Baseline flux	0.999789 ± 0.000089	$0.999799^{+0.000090}_{-0.000089}$
$F_0, \text{LCO UT 2460-35-2. (i')}$	Baseline flux	0.99999 ± 0.00021	1.00000 ± 0.00021
$F_0, \text{LCO UT 2460-40-5. (i')}$	Baseline flux	0.999933 ± 0.000084	$0.999936^{+0.000085}_{-0.000086}$
$F_0, \text{LCO UT 2460-42-4. (i')}$	Baseline flux	$1.000024^{+0.000099}_{-0.000098}$	1.000030 ± 0.000099
$F_0, \text{LCO UT 2460-42-9. (i')}$	Baseline flux	0.99963 ± 0.00012	0.99964 ± 0.00012



(a) The 5σ detection limit (contrast curve) for speckle interferometric observation of TOI-6884 with speckle polarimeter at SAI 2.5-m telescope. The inset panel shows the autocorrelation function.



(b) The contrast curves at 562 nm (blue curve) and 832 nm (red curve) measured from the reconstructed speckle images taken with NESSI at the WIYN 3.5 m telescope. The reconstructed speckle images are also shown as insets on the plot.

Figure A1. Speckle interferometric contrast curves for TOI-6884 obtained from two independent instruments: observations from the SAI 2.5-m telescope (top) and from the NESSI instrument on the WIYN 3.5-m telescope (bottom) (see Section 2.5).

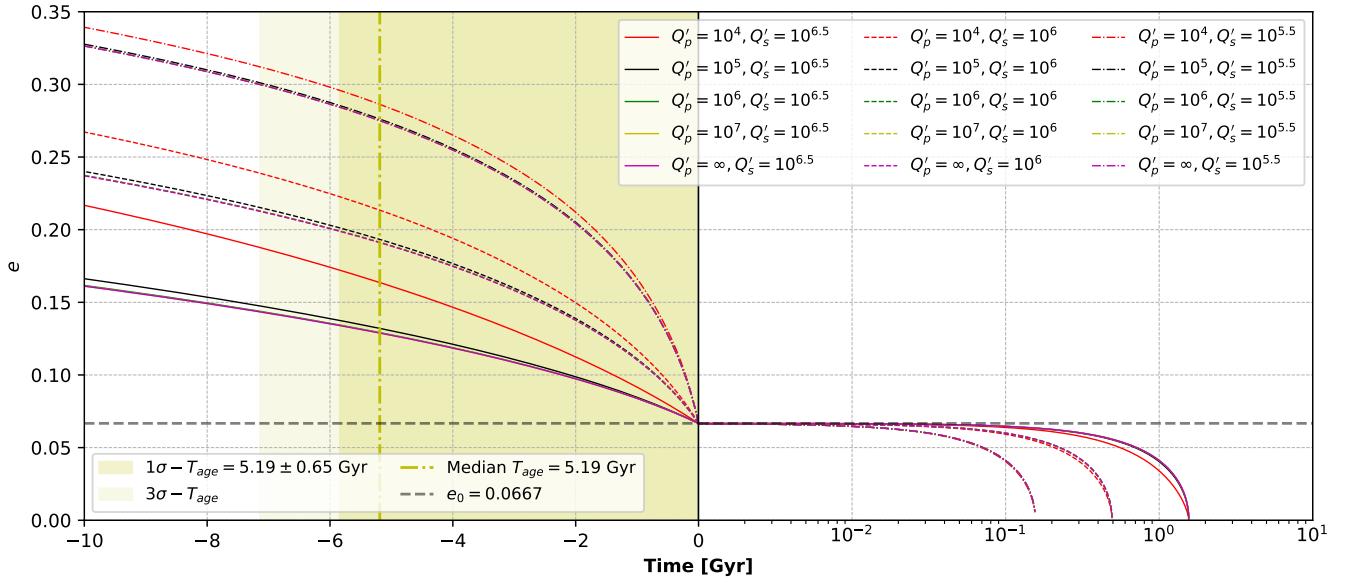


Figure A2. Backward and forward evolution of the orbital separation for different values of Q'_\star and Q'_p , based on the formulation of [Jackson et al. \(2009\)](#), for the low-probability solution of the TOI-6884 system. The high-probability solution is shown in Fig. 12.